



1  
2 **Toward an Observation-Based Estimate of Dust Net Radiative**  
3 **Effects in Tropical North Atlantic Through Integrating Satellite**  
4 **Observations and In Situ Measurements of Dust Properties**

5  
6 Qianqian Song<sup>1,2</sup>, Zhibo Zhang<sup>1,2\*</sup>, Hongbin Yu<sup>3</sup>, Seiji Kato<sup>4</sup>, Ping Yang<sup>5</sup>, Peter Colarco<sup>3</sup>,  
7 Lorraine A. Remer<sup>2</sup>, Claire L. Ryder<sup>6</sup>  
8

- 9 1. Physics Department, University of Maryland Baltimore County  
10 2. Joint Center for Earth Systems Technology, University of Maryland Baltimore County  
11 3. NASA Goddard Space Flight Center  
12 4. NASA Langley Research Center.  
13 5. Dept. of Atmospheric Sciences, Texas A&M University  
14 6. Department of Meteorology, University of Reading, RG6 6BB, UK.  
15  
16  
17

18 Send Correspondence to:

19 Dr. Zhibo Zhang

20 Email: [zhibo.zhang@umbc.edu](mailto:zhibo.zhang@umbc.edu)  
21  
22  
23  
24  
25  
26  
27



## Abstract

In this study, we integrate recent aircraft measurements of dust microphysical and optical properties with satellite retrievals of aerosol and radiative fluxes to quantify the dust direct radiative effects on the shortwave (SW) and longwave (LW) radiation (denoted as  $DRE_{SW}$  and  $DRE_{LW}$ , respectively) at both the top of atmosphere (TOA) and surface in the tropical North Atlantic during summer months. Through linear regression of CERES measured TOA flux versus satellite aerosol optical depth (AOD) retrievals under cloud-free and dust-laden atmospheric conditions, we estimate the instantaneous  $DRE_{SW}$  efficiency at the top of the atmosphere (TOA) to be  $-49.7 \pm 7.1$  W/m<sup>2</sup>/AOD and  $-36.5 \pm 4.8$  W/m<sup>2</sup>/AOD based on AOD from MODIS and CALIOP, respectively. The corresponding  $DRE_{SW}$  at TOA is  $-14.2 \pm 2.0$  W/m<sup>2</sup> and  $-10.4 \pm 1.4$  W/m<sup>2</sup>, respectively. We also estimate the instantaneous  $DRE_{LW}$  at TOA to be between  $+2.7 \pm 0.32$  W/m<sup>2</sup> to  $+3.4 \pm 0.32$  W/m<sup>2</sup> based on the difference between computed dust-free outgoing longwave radiation (OLR) and CERES-measured OLR. We then perform various sensitivity studies with recent measurements of dust particle size distribution (PSD), refractive index, and particle shape distribution to determine how the dust microphysical and optical properties affect DRE estimates and its agreement with abovementioned satellite-derived DREs. Our analysis shows that a good agreement with the observation-based estimates of instantaneous  $DRE_{SW}$  and  $DRE_{LW}$  can be achieved through a combination of recently observed PSD with substantial presence of coarse particles, a less absorptive SW refractive index, and spheroid shapes. Based on this optimal combination of dust physical and optical properties we further estimate the diurnal mean dust  $DRE_{SW}$  efficiency of  $-28$  W/m<sup>2</sup>/AOD at TOA and  $-82$  W/m<sup>2</sup>/AOD at surface. The corresponding TOA and surface  $DRE_{SW}$  in the region is approximately  $-10$  W/m<sup>2</sup> and  $-26$  W/m<sup>2</sup>, respectively, of which ~30% is canceled out by the positive  $DRE_{LW}$ . This yields a net DRE of about  $-6.9$  W/m<sup>2</sup> and  $-18.3$  W/m<sup>2</sup> at TOA and surface, respectively. Our study suggests that the LW flux contains



52 useful information of dust particle size, which could be used together with SW observation to

53 achieve more holistic understanding of the dust radiative effect.

54

55



## 56 1. Introduction

57 Mineral dust is the most abundant atmospheric aerosol component in terms of dry mass  
58 [Choobari *et al.*, 2014, Textor *et al.*, 2006]. The Sahara is the largest source of atmospheric dust  
59 aerosols, with an estimated emission of 670 Mt yr<sup>-1</sup> [Rajot *et al.*, 2008, Washington *et al.*, 2003].  
60 African dust from Sahara is regularly lifted by strong near-surface winds and transported  
61 westwards within the Saharan Air Layer (SAL) over to the tropical North Atlantic (see Figure 1)  
62 during northern summer [Cuesta *et al.*, 2009, Karyampudi *et al.*, 1999]. During the transport, dust  
63 aerosols can scatter and absorb both shortwave solar (referred to as “SW”) and longwave thermal  
64 infrared (referred to as “LW”) radiation, and thereby influence Earth’s energy budget [McCormick  
65 *et al.*, 1967, Tegen *et al.*, 1996, Yu *et al.*, 2006] . This is known as the direct radiative effect (DRE).  
66 In addition, mineral dusts can also influence the life cycle and properties of clouds, by altering  
67 thermal structure of the atmosphere (known as semi-direct effects) [Ackerman *et al.*, 2000, Hansen  
68 *et al.*, 1997, Koren *et al.*, 2004], and by acting as cloud condensation nuclei and ice nuclei (known  
69 as indirect effects) [Albrecht, 1989, Rosenfeld *et al.*, 1998, Twomey, 1977] . In addition, when  
70 African dust aerosols are deposited into Atlantic Ocean and Amazon Basin, they supply essential  
71 nutrients for the marine and rainforest ecosystems [Yu *et al.*, 2015], which has important  
72 implications for the biogeochemical cycles [Jickells *et al.*, 2005]. In this study, we focus on the  
73 quantification of dust direct radiative effect on both SW and LW radiation.

74 Substantial effort has been made to understand and quantify the DRE of mineral dust since  
75 the 1980s [Carlson *et al.*, 1980, Cess, 1985, Liao *et al.*, 1998, Ramaswamy *et al.*, 1985]. Most  
76 studies have focused on the SW DRE (DRE<sub>sw</sub>) of mineral dust under clear-sky (cloud free)  
77 conditions [Myhre *et al.*, 2003, Tegen *et al.*, 1996, Yu *et al.*, 2006] . Through scattering and  
78 absorption, dust aerosols reduce the amount of solar radiation reaching the surface, inducing a



negative (cooling) effect at the surface. The  $DRE_{sw}$  of dust at the top of the atmosphere (TOA) depends also strongly on the albedo of the underlying surface [Keil *et al.*, 2003, Yu *et al.*, 2006]. Over a dark surface, the scattering effect of dust dominates, which yields a cooling effect at TOA [Myhre *et al.*, 2003, Tegen *et al.*, 1996]. In contrast, high reflectance of a bright surface enhances the absorption by dust aerosols and could yield a positive (warming) dust  $DRE_{sw}$  at TOA when the surface albedo exceeds a critical value [Zhang *et al.* 2006]. Different from other aerosol types (e.g., smoke and sulfate aerosols), dust aerosols are large enough to have significant LW direct radiative effect ( $DRE_{LW}$ ) [Sokolik *et al.*, 1999, Sokolik *et al.*, 1998]. Lofted dust aerosols absorb the LW radiation from the warm surface and re-emit the LW radiation usually at lower temperature, thereby reducing the outgoing LW radiation and leading to a warming effect at TOA. At the same time, they emit the LW radiation downward that generates a warming effect at the surface. The dust LW effect depends strongly on surface emissivity and the vertical profile of atmosphere temperature. The net radiative effect ( $DRE_{net}$ ) of dust is the summation of its  $DRE_{sw}$  and  $DRE_{LW}$ . Note that  $DRE_{sw}$  only acts during daytime, whereas  $DRE_{LW}$  operates during both day and night.

Quantification of the  $DRE_{sw}$  and  $DRE_{LW}$  of dust remains challenging and there is a large range of estimates in the literature. Take the Tropical Atlantic for example. Yu *et al.* [2006] found that the seasonal (JJA) average clear-sky aerosol  $DRE_{sw}$  at TOA in this region varies from  $-5.7$   $W/m^2$  to  $-12.8$   $W/m^2$  based on observations and from  $-3.7$   $W/m^2$  to  $-10.4$   $W/m^2$  based on model simulations. An important reason is that dust DRE depends on many factors, including both the microphysical (e.g., dust particle size and shape) and optical (e.g., refractive index) properties, as well as the surface and atmospheric properties (e.g., surface reflectance and temperature, atmospheric absorption). Sokolik *et al.* [1998] showed that for the sub-micron dust particles, the  $DRE_{sw}$  is dominant and  $DRE_{LW}$  is negligible, whereas for super-micron dust particles,  $DRE_{LW}$  is



more important [Sokolik *et al.*, 1996, Sokolik *et al.*, 1999]. Therefore, an accurate measurement of the particle size distribution (PSD) is highly important for estimating the DRE of dust. However, observations of dust PSD are relatively scarce and subjected to large uncertainties [Mahowald *et al.*, 2014]. PSD inferred from AERONET observations [Dubovik *et al.*, 2006] relies on observations at shortwave channels, which could bias the dust size low. In fact, more and more observations are emerging to suggest that dust PSD even in regions far from source regions contains substantial fraction of coarse particles. Based on the airborne in-situ measurement of dust PSD in Caribbean Basin from the Puerto Rico Dust Experiment (PRIDE) campaign, Maring *et al.* [2003] noted that dust particles appear to settle more slowly than expected from the widely used Stokes gravitational settling model. Similarly, recent measurements from the latest Fennec project [Ryder *et al.*, 2013b] and the Saharan Aerosol Long-range Transport and Aerosol-Cloud-interaction Experiment (SALTRACE) [Weinzierl *et al.*, 2017] all suggest that transported dust aerosols in the SAL are significantly coarser than expected based on the Stokes gravitational deposition. Such unexpected existence of coarse particles has important implications for understanding the DRE of dust. In a case of significant fraction of coarse particles, the warming effect on LW radiation (positive)  $DRE_{LW}$  would partly cancel the  $DRE_{sw}$  leading to a less negative or even positive  $DRE_{net}$ . Most recently, Kok *et al.* [2017] argue that most of the current global climate models tend to underestimate the size of dust particles and therefore overestimate the cooling effects of dust. Their estimate of the global mean dust  $DRE_{net}$  is between  $-0.48$  and  $+0.20$   $W\ m^{-2}$ , which includes the possibility that dust causes a net warming of the planet.

In addition to dust particle size, particle shape and refractive index also have significant influence on dust DRE. Dust particles are generally nonspherical in shape, which make their single-scattering properties (i.e., extinction efficiency, single-scattering albedo and scattering



125 phase matrix) fundamentally different from those based on spherical models. A few dust particle  
126 shape models have been developed [Dubovik *et al.*, 2006, Kandler *et al.*, 2009], which have been  
127 increasingly used in aerosol remote sensing and modeling [Levy *et al.*, 2007]. Räisänen *et al.* [2013]  
128 found that replacing the spherical dust models in a GCM with nonspherical model leads to  
129 negligible changes in the DRE of dust at TOA. However, a recent GCM-based study by Colarco  
130 *et al.* [2014] suggests that the influence of nonsphericity on dust DRE can be significant at surface  
131 and within the atmosphere, depending on the refractive index of dust. Similarly, Kok *et al.* [2017]  
132 argue that a spherical model significantly underestimates the extinction of dust, leading to errors  
133 in estimate of dust DRE.

134 Over the past few decades, substantial efforts have been made to measure the spectral  
135 refractive index of dust, mostly limited to the SW spectral range [Balkanski *et al.*, 2007, Dubovik  
136 *et al.*, 2002, Dubovik *et al.*, 2006, Formenti *et al.*, 2011, Hess *et al.*, 1998, Levoni *et al.*, 1997].  
137 The current widely-used LW refractive index of dust was measured using rather old techniques in  
138 the 1970s and 1980s [e.g., Volz 1972, 1973, Fouquart *et al.* 1987]. Recently, Di Biagio *et al.* [2014,  
139 2017] compiled a comprehensive dust aerosol refractive index database in the LW spectrum  
140 ranging from 3 to 15  $\mu\text{m}$ , based on 19 natural samples from 8 dust regions over the globe. This  
141 database is the first one as far as we know to document the regional differences in dust LW  
142 refractive index due to the regional characteristics of dust chemical composition. We also call  
143 special attention to a newly developed database of Saharan and Asian dust [Stegmann and Yang,  
144 2017].

145 Satellite observations have long become indispensable for studying the dust aerosols. In  
146 particular, the combination of passive (e.g., MODIS and CERES) and active (e.g., CALIPSO)  
147 sensors on board of NASA's A-Train satellite constellation provides unprecedented data to study



dust aerosols, from long range transport [e.g., *Liu et al. 2008, Yu et al. 2015*] to dust DRE [e.g.,  
*Yu et al. 2006, Zhang et al. 2016*]. As A-Train observations become mature, substantial efforts  
have been made to collocate and fuse the observations from different sensors to make the use of  
A-Train observations easier for the users. A prominent example is the CERES- CALIPSO-  
CloudSat -MODIS (CCCM) product developed by Kato et al. [2011], which has become a popular  
dataset for studying the radiative effects of clouds and aerosols and for evaluating GCMs.

The present study is inspired and motivated by the latest measurements of the  
microphysical and optical properties of dust, namely the in-situ dust PSD from the Fennec field  
campaign [Ryder et al. 2013a, 2013b] and the dust LW refractive index from Di Biagio [2014,  
2017], as well as the recent studies (e.g., Kok et al.[2017]) suggesting that cooling effects of dust  
is overestimated in most climate models due to the underestimation of dust size. The study is  
carried out in three steps, each with a distinct objective. First, we attempt to derive a set of  
observation-based *instantaneous* dust  $DRE_{SW}$  and  $DRE_{LW}$  for the tropical North Atlantic based on  
the A-Train satellite observations reported in the CCCM product, without imposing any  
assumptions on dust size, shape or refractive index. Then, we perform multiple sets of radiative  
transfer computations of the *instantaneous* dust DRE in the North Atlantic region based on the  
same dust extinction profiles from CCCM in combination with different dust physical and optical  
properties. The objective is to understand the sensitivity of dust  $DRE_{SW}$  and  $DRE_{LW}$  to the PSD,  
nonsphericity, and refractive index of dust and to obtain a set of dust properties that yield the best  
agreement with satellite flux observations (e.g., CERES). In the third step, we use the derived dust  
properties and extend the radiative transfer computations to *diurnal mean* and to DRE at surface.  
The rest of this paper is organized as follows: Section 2 describes the data and model used. Section  
3 presents the sensitivity of dust DRE to dust size, shape and refractive index. Section 4 discusses





diurnally averaged net DRE of dust aerosols and uncertainty analysis. Section 5 concludes the article.

173

## 174 **2. Data and Models**

### 175 **2.1 The CERES- CALIPSO-CloudSat -MODIS (CCCM) product**

To estimate instantaneous dust DRE, we use aerosol and radiation remote sensing products from the A-Train satellite sensors, namely, the integrated CERES, CALIPSO, CloudSat, MODIS merged product (CCCM) developed by [Kato *et al.*, 2011]. In the CCCM product, high-resolution CALIOP, CloudSat and MODIS retrievals are collocated with 20-km CERES footprints. For each CERES footprint, the CCCM product provides the TOA flux observations (both SW and LW) from CERES, aerosol (MOD04 “Dark Target” product [Remer *et al.*, 2005] and cloud (MOD06 [Platnick *et al.*, 2003]) properties retrieved from MODIS, aerosol optical thickness for each aerosol layer from CALIOP [Winker *et al.*, 2010] and cloud vertical profile from the combination of CALIOP and CloudSat [Kato *et al.*, 2010]. Up to 16 aerosol layers identified by CALIOP are kept within a CERES footprint. Figure 1 shows the JJA mean aerosol optical depth (AOD) from the CALIOP observations reported in the CCCM product. Clearly, the transported dust aerosols lead to enhanced AOD in the tropical North Atlantic region.

In addition to the “raw” retrievals, the CCCM product also provides post-processed flux computations for each CERES pixel based on derived aerosol and/or cloud extinction profiles, which is done in the following steps. First, the CALIOP aerosol retrievals within each CERES pixel are averaged to obtain the aerosol extinction profile at the 0.5  $\mu\text{m}$  reference wavelength. Then, the aerosol type and associated spectral optical properties, e.g., extinction coefficient ( $\beta_e$ ), single-scattering albedo ( $\omega$ ), asymmetry factor ( $g$ ), are specified mostly based on the aerosol type simulations from the Model of Atmospheric Transport and Chemistry (MATCH [Collins *et al.*,



2001], with the exception of dust aerosols. If CALIOP observes dust aerosols (dust and polluted dust), the aerosol type is set to dust. This is based on the consideration that the depolarization observation capability of CALIOP is ideal for dust detection because the nonsphericity of dust can cause significant depolarization in contrast to most other types of aerosols. Finally, the aerosol extinction profiles and the aerosol spectral optical properties are used to compute the broadband fluxes at both TOA and surface and for both SW and LW under 2 conditions: 1) with aerosol, 2) without aerosol, so that the aerosol DRE can be derived from the difference of the two conditions. Temperature and humidity profiles used in flux computations are from the Goddard Earth Observing System (GEOS-5) Data Assimilation System reanalysis [Rienecker *et al.*, 2008].

204

## 2.2 Dust Physical and Optical models

To investigate the sensitivity of dust DRE to microphysical and optical properties of particles, we use several sets of widely used or newly obtained dust size distribution, dust shape distribution and dust refractive index.

Two dust particle size distributions (PSD) shown in Figure 2, are considered in this study. One PSD is inferred based on AERONET ground-based retrievals at Cape Verde site (16°N, 22°W) from [Dubovik *et al.*, 2002] (referred to as “AERONET” PSD). The other dust PSD is obtained from the recent airborne measurements of transported Saharan dust from the Fennec 2011 field campaign over both the Sahara (Mauritania and Mali) and the eastern Atlantic Ocean, between the African coast and Fuerteventura. Ryder *et al.* [2013a] separate the PSD measurements from this campaign into three broad categories: fresh, aged, SAL (acronym for “Saharan Air Layer”). The fresh category over the Sahara represents dust uplifted no more than 12 hours prior to measurement; the aged category over the Sahara represents dust aerosols mobilized 12 to 70 hours prior to



measurement; the SAL category represents dust aerosols transported over the adjacent east Atlantic, mostly from flights over Fuerteventura, Canary Islands (28°N, 13°W). All these categories come from the mean of vertical profile observations (excluding the marine boundary layer for SAL categories). The Fennec airborne PSD dataset is particularly novel, in that larger particle sizes were measured than has been done previously in dust layers, with the exception of Weinzierl et al., 2011, and that errors due to sizing uncertainties have been specifically quantified (see Ryder et al., 2013b and Ryder et al., 2015 for full details). Because this paper focuses on the Tropical Atlantic Ocean region, we use dust size distribution in the SAL category (referred to as the “Fennec-SAL PSD”). Evidently from Figure 2, the Fennec-SAL PSD, which peaks around 5~6  $\mu\text{m}$  and has a significant fraction of particles with  $r > 10\mu\text{m}$ , is much coarser than the AERONET PSD, which peaks around 1~2  $\mu\text{m}$  and has almost no particles  $r > 10\mu\text{m}$ .

The dust refractive indices are taken from three sources:

(1) The Optical Properties for Aerosols and Clouds database (OPAC) [Hess et al., 1998], which has been widely used in climate models and satellite remote sensing algorithms.

(2) A merger of remote sensing based estimates of dust refractive indices in the shortwave from 0.5  $\mu\text{m}$  to 2.5  $\mu\text{m}$  [Colarco et al., 2014], drawn from Kim et al. [2011] in the visible, and Colarco et al. [2002] in the UV and (referred to as “Colarco-SW”). Kim [2011] collected the AERONET (V 2) retrievals from 14 sites over North Africa and the Arabian Peninsula. Then the dust refractive index is derived from the dust dominant cases for these sites selected based on the combination of large aerosol optical depth ( $\text{AOD} \geq 0.4$  at 440 nm) and small Ångström exponent ( $\text{Å}_{\text{ext}} \leq 0.2$ ) to select the dust cases. Colarco et al. [2002] derived the dust refractive index in the UV by matching the simulated dust radiative signature in the UV with the satellite observations from the Total Ozone Mapping Spectrometer.



241 (3) The refractive indices in the LW from  $3\mu\text{m}$  ~ $15\mu\text{m}$  from Di Biagio et al. [2017]  
242 (referred to as “Di-Biagio-LW”). This database is based on the laboratory measurements of 19  
243 natural soil sample from 8 regions: northern Africa, the Sahel, eastern Africa and the Middle East,  
244 eastern Asia, North and South America, southern Africa, and Australia. The refractive index from  
245 the Mauritania site is selected for this study because it is geographically close to the Fennec field  
246 campaign.

247 Figure 3 compares the real and imaginary parts of the refractive index for each of these  
248 data sets. In the SW, the imaginary part of the OPAC refractive index is much greater than that of  
249 Colarco-SW, which implies that dust aerosols based on the OPAC refractive index is more  
250 absorptive. In the LW, the Di-Biagio-LW refractive index is smaller than the OPAC values in  
251 terms of both the real and imaginary parts.

252 Dust aerosols are generally nonspherical in shape. Spheroids have proven to be a  
253 reasonable first-order approximation of the shape of nonspherical dust [Dubovik et al., 2006,  
254 Mishchenko et al., 1997]. The shape of a spheroid particle is determined by the so-called aspect  
255 ratio, i.e., ratio of the polar to equatorial lengths of the spheroid. In our study, two spheroidal shape  
256 distributions are used for computing the optical properties of non-spherical dust: (1) a size-  
257 independent aspect ratio distribution from Dubovik et al. [2006] (see Figure 4a) and (2) a size-  
258 dependent aspect ratio distribution extracted from Table 2 in Koepke et al. [2015], which is  
259 discretized from measurement data of Kandler et al. [2009] (Figure 4b). The Dubovik et al. [2006]  
260 shape distribution employs both oblate (aspect ratio  $< 1$ ) and prolate (aspect ratio  $> 1$ ) spheroids,  
261 while the Kandler et al. [2009] shape distribution considers only prolate spheroids. For comparison  
262 purpose, we also include spherical dust in our sensitivity studies. We use the Lorenz-Mie theory  
263 code of Wiscombe [1980] to compute the optical properties of spherical dust particles. The optical



properties of spheroidal dust particles are derived from the database of Meng et al. [2010]. Note that we assume volume equivalent radius for the AERONET-PSD to be consistent with Dubovik et al. [2006] and the maximum dimension for Fennec-SAL PSD to be consistent with Ryder et al. [2013b].

### 2.3 Radiative transfer modeling

The Rapid Radiative Transfer Model (RRTM) [Mlawer et al., 1997] is used to compute both SW and LW radiative fluxes for both clear and dusty atmospheres. RRTM retains reasonable accuracy in comparison with line-by-line results for single column calculations. It divides the solar spectrum into 14 continuous bands ranging from  $820\text{cm}^{-1}$  to  $50000\text{cm}^{-1}$  and the thermal infrared ( $10\text{--}3250\text{cm}^{-1}$ ) into 16 bands. We explicitly specify the spectral AOD,  $\omega$  and  $g$  of dust aerosols for every band in the radiative transfer simulations.

## 3. Case Selection and Observation-based Estimate of Dust DRE

### 3.1 Selection of cloud-free and dust-dominant cases in the CCCM product

In this study, we focus on the Saharan dust outflow region in North Atlantic marked by the box in Figure 1 ( $10^\circ\text{N} \sim 30^\circ\text{N}$ ,  $45^\circ\text{W} \sim 20^\circ\text{W}$ ). This selection is based on several considerations. Firstly, during the summer months (JJA) this region is dominated by transported dust aerosols from Sahara. Secondly, because the ocean surface is dark, dust aerosols have a strong negative DRE<sub>sw</sub> in this region. Thirdly, the abovementioned AERONET Cape Verde and Fennec-SAL PSD measurements are made in the vicinity of this region. Finally, the dust DREs in this region have been extensively studied in the literature, making it easier for us to compare our results with previous work.



We first select cloud-free and dust-dominant CERES pixels in the region from five summer seasons (2007~2011) of the CCCM product. The MODIS and CALIOP cloud mask data are used first to select cloud-free CERES pixels. Then, within the cloud-free CERES pixels, we use the aerosol type information in the CCCM product to further select dust-dominant cases (i.e., more than 90% of the aerosols within a given CERES pixel are attributed to dust, in terms of area coverage). As aforementioned, the CCCM product relies on CALIOP observations, instead of ancillary data from MATCH, for detecting dust aerosols. Because of the relative large footprint size (~20 km), the cloud-free condition actually poses a strong constraint on the CERES product. Out of the 36165 of CERES pixels in this region from 5 seasons of data, we found 1663 (only 5%) of cloud-free pixels according to sub-pixel MODIS and CALIOP observations. After imposing the dust-dominant condition, we are left with a total of 607 cloud-free and dust-dominant CERES pixels. Furthermore, we found that within these selected pixels 153 cases have both CALIOP and MODIS aerosol optical depth (AOD) retrievals in the CCCM product and the rest (454 cases) have AOD retrievals only from the CALIOP.

300

### 3.2 Observation-based estimate of instantaneous dust DRE

Many previous studies have shown that the aerosol DRE<sub>sw</sub> over the dark ocean surface is approximately linear with the AOD. The increasing rate of the magnitude of DRE<sub>sw</sub> with AOD is called the DRE<sub>sw</sub> efficiency which is an important and useful quantity in many applications such as aerosol model evaluation [Zhou *et al.*, 2005]. Because of the nearly linear relationship between DRE<sub>sw</sub> and AOD, the CERES TOA flux observation and the collocated AOD retrievals from either CALIOP or MODIS can be combined to derive an observation-based estimate of the instantaneous dust DRE. Figure 5 shows linear regressions of CERES measured upward SW flux



309 at TOA with satellite retrieved AOD for the selected cloud-free and dust dominant cases. For the  
310 153 cases with both CALIOP and MODIS AOD retrievals, the combination of CERES and  
311 MODIS (Figure 5a) leads to a  $DRE_{sw}$  efficiency of dust  $-49.7 (\pm 7.1) \text{ W/m}^2/\text{AOD}$  (AOD is at  $0.5$   
312  $\mu\text{m}$ ) with a linear regression  $R^2$  value of  $0.69$ . The uncertainty, i.e.,  $\pm 7.1 \text{ W/m}^2/\text{AOD}$ , associated  
313 with the regression line coefficients is estimated based on the  $1-\sigma$  (one standard deviation) errors  
314 following [Hsu *et al.*, 2000]. While the combination of CERES and CALIOP (Figure 5b) leads to  
315 a  $DRE_{sw}$  efficiency at  $-29.6 \text{ W/m}^2/\text{AOD}$  with  $R^2$  value at  $0.27$ . Obviously, the difference is due to  
316 the difference in AOD retrievals. The tighter correlation between MODIS AOD and TOA upward  
317 SW flux is expected because MODIS retrieval is based on the reflected spectral solar radiation,  
318 whereas the CALIOP AOD retrievals are based on the inversion of backward scattering lidar  
319 signals. Nevertheless, if the other 454 cases with only CALIOP AOD retrievals are also included  
320 in the regression, the  $R^2$  value increases to  $0.5$  and the  $DRE_{sw}$  efficiency increases to  $-36.5 (\pm 4.8$   
321 based on  $1-\sigma$  error)  $\text{W/m}^2/\text{AOD}$  (Figure 5c). The reasons for the differences between CALIOP  
322 and MODIS AOD retrievals are beyond the scope of this study. Here, we conclude that the  
323 *instantaneous* dust  $DRE_{sw}$  efficiency in the selected region during summer season is  $-49.7 \pm 7.1$   
324  $\text{W/m}^2/\text{AOD}$  based on CERES-MODIS observations and  $-36.5 \pm 4.8 \text{ W/m}^2/\text{AOD}$  based on  
325 CERES-CALIOP observations. With the  $DRE_{sw}$  efficiency the  $DRE_{sw}$  can be easily derived from  
326 the AOD observations. The *instantaneous*  $DRE_{sw}$  estimated from the CERES-MODIS and  
327 CERES-CALIOP data is  $-14.2 \pm 2.0 \text{ W/m}^2$  and  $-10.4 \pm 1.4 \text{ W/m}^2$ , respectively. (see Table 1).

328 In addition to the SW flux measurement, the CCCM product also provides the CERES  
329 measurement of LW flux at TOA. Figure 6 shows the histograms of the broadband outgoing  
330 longwave radiation (OLR) measured by CERES for the selected cases. Note that besides dust AOD,  
331 OLR also strongly depends on other factors such as surface temperature, atmospheric profiles and



dust altitude. As a result, there is a high variability in those abovementioned factors among the selected 607 cases. Therefore, it is not possible to derive the  $DRE_{LW}$  efficiency in the same way as  $DRE_{SW}$  efficiency. To estimate the  $DRE_{LW}$ , we computed dust-free OLR based on ancillary data of surface temperature and atmospheric profiles from the CCCM. Then, the  $DRE_{LW}$  can be estimated from the difference between CERES observed OLR (i.e., blue solid line in Figure 6) and the computed dust-free OLR (i.e., black dashed line in Figure 6). To test if our computed dust-free OLR has any potential bias due to, for example, errors in the ancillary data (i.e., atmospheric gas and temperature), we selected 75 cloud free cases in the same region and season with no dust detected by CALIPSO. Note that because of the small dust loading in these cases the computed OLR at TOA mainly depends on the accuracy of ancillary data of surface temperature and atmospheric profiles. Therefore, the comparison between the computed OLR and CERES measurements of those cases can inform us if there is any potential bias in our computation of dust-free OLR. It turns out that the difference between RRTM and CERES OLR has a mean value around  $0.7 \text{ W/m}^2$  with standard deviation around  $3.8 \text{ W/m}^2$  (not shown). This result does not necessarily mean that our dust-free OLR computation has a positive  $0.7 \text{ W/m}^2$  bias, because of the sampling difference between the dust-free and dust-laden cases. Here we consider it as potential uncertainty. In the analysis followed we estimate two sets of semi-observation based  $DRE_{LW}$  under two assumptions: one is assuming zero bias in our OLR computation, the other one is assuming a positive  $0.7 \text{ W/m}^2$  bias. If we neglect the bias, by differentiating the dust-free OLR computed by RRTM and the CERES-measured OLR we are able to derive a mean semi-observation-based *instantaneous*  $DRE_{LW}$  of dust at  $3.4 \pm 0.32 \text{ W/m}^2$  with the 95% confidence level. If we assume there is a positive  $0.7 \text{ W/m}^2$  in RRTM computed dust-free OLR, by the same way we are able to





354 get a mean semi-observation-based *instantaneous* DRE<sub>LOW</sub> of dust at  $2.7 \pm 0.32$  W/m<sup>2</sup> with 95%  
355 confidence level.

## 356 **4. Sensitivity of Dust DRE to Microphysical and Optical Properties of** 357 **Particles**

358 The cloud-free and dust-laden cases from the CCCM product facilitate an ideal testbed for  
359 investigating the sensitivity of dust DREs to the microphysical (i.e., PSD and shape) and optical  
360 (i.e., refractive index) properties of dust. We use the aerosol extinction profiles at the 0.5  $\mu$ m from  
361 the CCCM product (which is based on CALIOP/CALIPSO observations) and different  
362 combinations of the dust properties to drive multiple sets of radiative transfer simulations of dust  
363 DREs. Through comparisons of the radiative transfer simulations with CERES observation, we  
364 study how the physical and optical properties influence both the DRE<sub>SW</sub> and DRE<sub>LOW</sub> of dust. It  
365 should be mentioned here that the CCCM product also use the same methodology to generate the  
366 aforementioned post-processed flux profile. In the analysis, we will also compare our dust DRE  
367 simulations with the results provided in the CCCM products.

### 368 **4.1 Sensitivity to dust size and refractive index**

369 In the first sensitivity study, we study the influences of dust size and refractive index on  
370 the dust scattering properties and consequently dust DREs. Based on different combinations of the  
371 PSDs (AERONET vs. Fennec-SAL) and SW refractive index (OPAC vs. Colarco-SW), we  
372 simulate four sets dust spectral scattering properties (Figure 7), and correspondingly four sets of  
373 dust DRE<sub>SW</sub> efficiency (Figure 8). In the simulations, dust particles are assumed to be spheroidal  
374 and the aspect ratio distribution from Dubovik et al. [2006] (see Figure 4a) is used. The OPAC-



375 LW refractive index is used. The impacts of dust shape distribution and LW refractive index on  
 376 dust DRE will be discussed later.

377 Figure 7 shows the scattering properties for the four different combinations of dust PSD  
 378 and refractive index. The extinction efficiency ( $Q_e$ ) based on the Fennec-SAL PSD is significantly  
 379 larger than that based on the AERONET PSD (Figure 7a). The spectral shape is also different. The  
 380  $Q_e$  based on the Fennec-SAL PSD is rather flat in the SW region due to its large size whereas the  
 381  $Q_e$  based on the AERONET PSD decreases with wavelength. The  $Q_e$  shows no sensitivity to  
 382 refractive index in Figure 7a. It is because the Colarco-SW and OPAC-SW are different only in  
 383 the imaginary part (see Figure 3) which has minimal influence on  $Q_e$ . In contrast, the single  
 384 scattering albedo (SSA) in Figure 7b shows more sensitivity to refractive index. As expected, the  
 385 Fennec-SAL PSD and OPAC-SW combination (i.e., larger size and more absorptive refractive  
 386 index) has the smallest SW SSA while the AERONET PSD and Colarco-SW i.e., smaller size and  
 387 less absorptive refractive index) has the largest SW SSA. The other two combinations yield similar  
 388 SW SSA that are in between the abovementioned two extremes. The asymmetry factor ( $g$ ) in  
 389 Figure 7c shows a primary sensitivity to size and a secondary sensitivity to refractive index.

390 Figure 7d shows spectral variation of dust AOD normalized with respect to AOD at  $0.5\mu\text{m}$ .  
 391 The peak wavelength of solar radiation ( $0.5\mu\text{m}$ ) and peak wavelength of terrestrial thermal  
 392 radiation ( $10\mu\text{m}$ ) are highlighted with dashed lines. The  $0.5\mu\text{m}$  AOD is used as the reference for  
 393 normalization because as aforementioned, we use the  $0.5\mu\text{m}$  aerosol extinction profile in the  
 394 CCCM derived from CALIOP to drive our radiative transfer simulations. After spectral  
 395 normalization, one can see that given the same  $0.5\mu\text{m}$  AOD the  $10\mu\text{m}$  AOD based on the Fennec-  
 396 PSD is much larger than that based on the AERONET PSD by around 80%. This is an important  
 397 feature that has important implications for the  $\text{DRE}_{\text{LW}}$  of dust. The SW reflection of dust depend



not only on AOD, but also SSA and  $g$ . Figure 7e shows spectral variation of  $AOD \cdot SSA \cdot (1 - g)$ , where AOD indicates dust load, multiplied by SSA to take the scattered fraction, multiplied by  $1 - g$  to take the backscattered portion. It is a quantity more relevant for understanding dust SW reflection. Evidently, this index suggests that the combination of smaller size (AERONET PSD) and less absorptive refractive index (Colarco-SW) leads to most reflective dust among the four sets of simulations, whereas the larger size (Fennec PSD) and more absorptive refractive index (OPAC) combination generates least reflective dust. The other two combinations are in between and somewhat similar.

Figure 8 shows the four sets of simulated TOA upward SW fluxes as a function of the input AOD at  $0.5 \mu\text{m}$ . For comparison purpose, the  $DRE_{\text{sw}}$  efficiency regression results based on observations in Figure 5, as well as the results reported in the CCCM products, are also plotted. Focusing on our computations first, we note that as expected the most reflective dust based on the combination of AERONET PSD and Colarco-SW refractive index leads to the largest  $DRE_{\text{sw}}$  efficiency ( $-70.5 \text{ W/m}^2/\text{AOD}$ ), while the least reflective dust based on the combination of Fennec-SAL PSD and OPAC ref yields the smallest  $DRE_{\text{sw}}$  efficiency ( $-30.6 \text{ W/m}^2/\text{AOD}$ ). Clearly, these results are outside of the range based on observations (i.e.,  $-36.5 \pm 4.8 \sim -49.7 \pm 7.1 \text{ W/m}^2/\text{AOD}$ ), suggesting they are too extreme. The other two combinations, i.e. AERONET PSD+OPAC-SW and Fennec-SAL PSD + Colarco-SW, generate similar  $DRE_{\text{sw}}$  efficiency at  $-47.6$  and  $-53.3 \text{ W/m}^2/\text{AOD}$ , respectively, both comparable to the CERES-MODIS based value. Interestingly, the  $DRE_{\text{sw}}$  efficiency based on the flux computations reported in the CCCM product is  $-81 \text{ W/m}^2/\text{AOD}$ , even larger than that based on AERONET PSD + Colarco refractive index, suggesting that the dust model used in the CCCM flux computations is too reflective in the SW. The *instantaneous*  $DRE_{\text{sw}}$  and  $DRE_{\text{sw}}$  efficiency at surface for the two combinations that agree with



the CERES observation, i.e., AERONET PSD+OPAC-SW and Fennec-SAL PSD + Colarco-SW, are given in the Table 2.

On one hand, the results in Figure 8 are encouraging, as they suggest that a relatively simple combination of dust size and refractive index can enable us to simulate the dust DRE<sub>sw</sub> that are comparable with observations. On the other hand, the fact that two different dust models lead to similar DRE<sub>sw</sub> efficiency simulation, both comparable with observation, points to a long-lasting problem in aerosol remote sensing. That is, different combinations of aerosol microphysical and optical properties can lead to similar radiative signatures. The combination of smaller dust size with more absorptive refractive index is as good as the combination of larger size with less absorptive refractive index, as long as DRE<sub>sw</sub> is concerned.

But are the two combinations also equal in terms of closing the LW radiation? This is an important question, because ideally an appropriate dust model should close both SW and LW radiation. To address this question, we extend our radiative transfer simulations to the LW. It is important to point out that the LW and SW dust radiative properties are not independent but related through the physical properties of dust. For example, the AOD at a given wavelength  $\lambda$  in LW is related to the visible AOD through

$$AOD(\lambda) = AOD(0.5\mu m) \frac{Q_e(\lambda)}{Q_e(0.5\mu m)}, \quad (1)$$

where  $Q_e$  is the extinction efficiency that is determined by dust size, shape and refractive index. The dust size and shape are obviously independent of wavelength and therefore connect the SW and LW. Even the refractive index in the SW and LW regions should be physically self-consistent because refractive index is determined by the chemical composition of dust. Unfortunately, because the refractive index measurements are often made either for SW only or LW only, there



442 is a lack of measurement of dust refractive index measurement from visible all the way to thermal  
443 infrared.

444 In our computations, we first use the LW dust refractive index from OPAC to compute the  
445 dust LW scattering properties and the corresponding OLR. Based on the same OPAC-LW  
446 refractive index, the Fennec-SAL PSD yields an instantaneous  $DRE_{LW}$  of  $+3.0 \text{ W/m}^2$  at TOA and  
447  $+7.7 \text{ W/m}^2$  at surface (see Table 3). The results based on the AERONET PSD are significantly  
448 smaller,  $+1.8 \text{ W/m}^2$  at TOA and  $+4.7 \text{ W/m}^2$  at surface. This difference between the two PSDs can  
449 be easily understood with Figure 7b. Given the same visible AOD, the coarser Fennec PSD has a  
450 larger infrared AOD than the AERONET PSD, and therefore stronger warming effects in the LW.

451 The more important question is which one, Fennec or AERONET PSD, leads to OLR  
452 simulations that agree better with the CERES observation? The differences between the computed  
453 OLRs and the CERES measurements of OLR for the selected dust cases are shown in Table 4,  
454 together with the significance test results, i.e., ‘t-score’ and ‘p-value’ from the Student’s t-test.  
455 Interestingly, the OLRs based on the combination of AERONET PSD + OPAC-LW refractive  
456 index are systematically warmer than CERES measurements by an average of  $1.6 \text{ W/m}^2$ . The high  
457 t-score of 4.2 and extremely low p-value of  $2.7\text{e-}5$  indicate this warm bias to be statistically  
458 significant. In contrast, the OLRs based on the combination of Fennec PSD + OPAC-LW refractive  
459 index have a bias only at  $0.5 \text{ W/m}^2$  and a p-value (0.23) significantly larger than the commonly  
460 used 0.05 threshold, which means that OLR of this dust model is very close to CERES  
461 measurements. Then, to investigate the sensitivity of the computation to LW dust refractive index,  
462 we performed the computations again based on the Di Biagio et al. LW refractive index. As shown  
463 in Table 4, the OLR based on Fennec PSD is still better than that based on the AERONET PSD,  
464 even though both sets deteriorate slightly in comparison with the results based on the OPAC LW



refractive index. Values in parentheses in Table 5 are derived based on the assumption of a positive  $0.7 \text{ W/m}^2$  bias in RRTM dust-free OLR. Evidently, the potential bias does not change our conclusion. Overall, the size difference is the primary reason for the fact that the OLR based on Fennec PSD is systematically colder than that based on the AERONET PSD. As shown in Figure 7, due to size difference, the  $Q_e$  based on the Fennec-SAL PSD (coarser) decreases at a slower rate than that based on the AERONET PSD (finer). As a result, according to Eq. (1) given the same SW AOD, the Fennec-SAL has a larger LW AOD and therefore colder OLR than the AERONET PSD. In comparison with our results, the OLRs reported in the CCCM product (not shown here) are on average  $3.1 \text{ W/m}^2$  warmer than CERES measurements. This warm OLR bias of CCCM product in the LW is consistent with its “too reflective” bias in the SW in Figure 8.

The LW result in Table 4 is interesting and important. First of all, it suggests that the LW spectral region provides useful information content on dust properties that is complementary to SW. As we see from Figure 8, the Fennec-SAL PSD + Colarco-SW refractive index and AERONET PSD + OPAC-SW SW refractive combinations yield very similar SW radiation simulations. However, only Fennec PSD can lead to reasonable LW radiation simulation. Secondly, although the main point here is more about the usefulness of the information content in LW, the fact that the coarser Fennec PSD leads to better OLR simulation than AERONET PSD and CCCM product (based on MATCH) aligns with the recent studies (e.g., Kok et al. [2017]) arguing that dust size tends to be underestimated in the aerosol simulation models.

Finally, as expected, the combination of Fennec PSD + OPAC-LW also yields the best simulation of the dust  $\text{DRE}_{\text{LW}}$ , at  $3.0 \text{ W/m}^2$ , in comparison with the result derived from the CERES OLR observations and RRTM dust-free OLR computation with ancillary data provided by CCCM product (i.e.,  $+3.4 \pm 0.32 \text{ W/m}^2$  based on CERES-CALIPSO combination).



488

489 **4.2 Sensitivity to dust shape**

490 In this section, we investigate the sensitivity of dust DRE to the shape (or shape distribution)  
491 of dust. For all the computations in the last section, we have used the spheroidal dust model with  
492 the aspect ratio distribution from Dubovik et al. [2006] (See Figure 4a). Now, we replace this  
493 model with another spheroidal dust model by Kandler et al. [2009] shown in Figure 4b. For  
494 comparison purpose, we also carry out another set of computation assuming spherical dust. For  
495 dust size and refractive index, we use the Fennec-SAL and Colarco-SW/OPAC-LW refractive  
496 index since dust DREs based on this combination has shown the best agreement with the  
497 observations.

498 In Figure 9, we compare the scattering properties of dust based on three different shape  
499 models. Overall, the two spheroidal models are very similar and both significantly different from  
500 the spherical model. More specifically, in the SW the  $Q_e$  based on spheroidal models is  
501 significantly larger than that based on spherical dust model. In the LW it is the opposite. The  $\omega$   
502 in Figure 9b suggest that the spherical dust is more absorptive than spheroidal dust in the SW  
503 region, when other things are equal. Figure 9d and e show the normalized the AOD with respect  
504 to  $AOD(0.5 \mu m)$  and the spectral variation of the scattering index  $AOD \cdot \omega \cdot (1 - g)$ . From Figure  
505 9d we can see that given the same SW AOD, the spherical model has the larger LW AOD than the  
506 two spheroidal models. The comparison in Figure 9e reveals that the spherical dust model is less  
507 reflective than the spheroidal model in the SW.

508 Figure 10 shows the radiative transfer simulations for the selected cases based on the three  
509 dust shape models. The  $DRE_{SW}$  efficiency based on the Kandler et al. [2009] is  $-48.3 \text{ W/m}^2/\text{AOD}$ ,  
510 which almost identical to the  $-47.6 \text{ W/m}^2/\text{AOD}$  based on the Dubovik et al. [2006] model. In



511 contrast, the  $DRE_{SW}$  efficiency based on the spherical dust model is much smaller  $-39.8$   
512  $W/m^2/AOD$ , which can be expected from the results in Figure 9e (i.e., spherical dust is less  
513 reflective). Table 6 shows the OLR computations based on different dust shape models. Again, the  
514 two spheroidal dust models yield very similar OLR simulations, they are both a little bit warmer  
515 than CERES OLR, while the results based on the spherical model is somewhat colder. This can be  
516 expected from the normalized  $Q_e$  plot in Figure 9d (AOD @  $10 \mu m$  for spherical dust model is  
517 larger than spheroidal dust model in the case of AOD @  $0.5 \mu m$  is constrained to be equal for both  
518 dust models). But all three sets of OLR simulations have a p-value larger than the 0.05 threshold,  
519 making it difficult to tell which dust shape model is better in terms of DREs study in this paper.  
520 Values in parentheses are also derived based on assumption of a positive  $0.7 W/m^2$  bias in RRTM  
521 computed dust-free OLR. With this assumption, spherical dust model has a large t-score ( $-2.1$ ) and  
522 p-value (0.033) smaller than threshold p-value 0.05. This means that the difference between  
523 RRTM and CERES OLR is statistically significant for spherical dust model with this assumption.  
524 Overall, spheroidal dust models agree well with CERES OLR no matter with assumption of  $0.7$   
525  $W/m^2$  bias in RRTM OLR or not. It needs to be pointed out that our computations concern only  
526 broadband flux at TOA. The two spheroidal models may have different angular and/or spectral  
527 signature in terms of radiance, which is more important for satellite remote sensing. But this is  
528 beyond the scope of this study and will be investigated in future work.

## 529 **5. Diurnally Mean Dust DRE in North Atlantic**

530 The DRE computations in the last section (i.e., Table 1~ Table 3) are *instantaneous* values  
531 corresponding to the overpassing time of Aqua around 1:30PM local time. The strong solar  
532 insolation makes the instantaneous  $DRE_{SW}$  much larger than  $DRE_{LW}$  in terms of magnitude,  
533 leading to a strong negative  $DRE_{net}$  (cooling) of dust. However, the  $DRE_{SW}$  operates only during





534 daytime, while the  $DRE_{LW}$  operates both day and night. In addition, because of the availability of  
535 satellite observations only at TOA, we have focused only on the DRE at TOA in the analyses  
536 above. To appreciate the relative magnitude of  $DRE_{LW}$  with respect to  $DRE_{SW}$  we extend our DRE  
537 simulations and analysis from *instantaneous* to *diurnal mean*, and also from TOA to surface. Over  
538 tropical ocean, the OLR is most sensitive to sea surface temperature (SST). Our sensitivity study  
539 based on the 3-hour MERRA (Modern-Era Retrospective analysis for Research and Applications)  
540 data suggests that the diurnal SST variation in the tropical North Atlantic region is so small that  
541 the diurnal mean OLR is close to the *instantaneous* value. Similarly, we also found that the diurnal  
542 variation of atmospheric profile (e.g., water vapor) has negligible impact on the diurnal  $DRE_{SW}$   
543 computation. Therefore, we only compute the diurnal variation of  $DRE_{SW}$  due to the change of  
544 solar zenith angle and ignore the small diurnal variation of  $DRE_{LW}$  as well as the impacts of  
545 atmospheric profile change on  $DRE_{SW}$ .

546 Table 6 summarizes the key results of the diurnal mean  $DRE_{SW}$  and  $DRE_{SW}$  efficiency at  
547 TOA, as well as at surface. In the SW, the two most reasonable combinations of PSD and refractive  
548 index, Fennec-SAL PSD + Colarco-SW and AERONET-PSD + OPAC-SW leads to similar TOA  
549  $DRE_{SW}$  efficiency around  $-29 \text{ W/m}^2/\text{AOD}$ , which is at the center of the  $-16 \sim -41 \text{ W/m}^2/\text{AOD}$   
550 range reported in Yu et al. [2006]. At the surface, the  $DRE_{SW}$  efficiency based on these two  
551 combinations are around  $-83 \text{ W/m}^2/\text{AOD}$ , which is significantly stronger than the  $-27 \sim -68$   
552  $\text{W/m}^2/\text{AOD}$  range reported in Yu et al. [2006]. It should be noted that we have limited this study  
553 to dust-dominant cases, whereas the values in Yu et al. [2006] are based on simple domain average  
554 and include other types of aerosol.

555 By combining the information in Table 3 and Table 6, we can easily derive the net  $DRE_{net}$   
556 of dust in the North Atlantic during summer. The TOA  $DRE_{net}$  based on the combination of



557 Fennec-SAL PSD + Colarco-SW + OPAC-LW refractive indices gives a regional mean  $DRE_{net}$  of  
558  $-6.9 \text{ W/m}^2$  and  $-18.3 \text{ W/m}^2$  at TOA and surface, respectively. In comparison, the corresponding  
559 values based on the combination of AERONET PSD + OPAC-SW + OPAC-LW refractive indices  
560 are  $-8.5 \text{ W/m}^2$  and  $-22.5 \text{ W/m}^2$ , respectively. It is interesting and important to point out that the  
561  $DRE_{LW}$  is significant, about 17% ~ 36% (depending on the choice of PSD and refractive index) in  
562 terms of magnitude with respect to the  $DRE_{sw}$ , and therefore not negligible in the  $DRE_{net}$   
563 regardless whether for TOA or surface.

## 564 6. Summary and Discussions

565 In this study, we use A-Train satellite observations reported in the CCCM product and  
566 recent in situ measurements of dust properties to investigate the DREs of the dust aerosols in the  
567 North Atlantic African dust outflow region during summer months. First, we select about 600  
568 cloud-free and dust-dominant CERES pixels from 5 seasons of CCCM product. Based on these  
569 cases, we first derive a set of observation-based instantaneous (corresponding to Aqua overpassing  
570 time)  $DRE_{sw}$  efficiency and  $DRE_{sw}$  using the combination of CERES-measured TOA flux and  
571 MODIS or CALIPSO retrieved dust AOD. The  $DRE_{sw}$  efficiency and  $DRE_{sw}$  based on CERES-  
572 MODIS observation are  $-49.7 \pm 7.1 \text{ W/m}^2/\text{AOD}$  and  $-14.2 \pm 2 \text{ W/m}^2$ , respectively. The values  
573 based on the CERES-CALIOP combination are  $-36.5 \pm 4.8 \text{ W/m}^2/\text{AOD}$  and  $-10.4 \pm 1.4 \text{ W/m}^2$ ,  
574 respectively. Using the combination of CERES-measured OLR (i.e., with dust) and computed  
575 dust-free OLR based on ancillary data, we also derive a set of semi-observation-based TOA  
576  $DRE_{LW}$  between  $2.7 \pm 0.32 \sim 3.4 \pm 0.32 \text{ W/m}^2$ .

577 In the follow-up sensitivity study, we use radiative transfer model to compute the DRE of  
578 dust using the observed  $0.5 \mu\text{m}$  dust extinction profiles from CALIPSO under various different



assumptions of dust PSD, refractive index and shape distributions. We find that two dust models, one based on Fennec-SAL PSD and Colarco-SW refractive index and the other on AERONET PSD and OPAC-SW refractive index, provide the best fit to the observation-based DRE<sub>sw</sub> efficiency and DRE<sub>sw</sub>. However, only the one based on the Fennec-SAL PSD, which is much coarser than the AERONET-PSD, can also provide reasonable fit to the observation-based DRE<sub>lw</sub>. We also find that the DREs based on the two spheroidal dust models are quite similar to each other, but more different from those based on spherical dust, suggesting that the detailed shape distribution is less important in the calculation of dust DRE. Based on the dust model that provides the best fit to the observation-based DRE, we estimate the diurnal mean dust DRE<sub>sw</sub> efficiency in the North Atlantic region during summer months to be around  $-28$  and  $-82$  W/m<sup>2</sup>/AOD at TOA and surface, respectively. The corresponding DRE<sub>sw</sub> is  $-9.9$  W/m<sup>2</sup> and  $-26$  W/m<sup>2</sup> at TOA and surface, respectively. The diurnal mean DRE<sub>lw</sub> is about  $3$  W/m<sup>2</sup> at TOA and  $7.7$  W/m<sup>2</sup> at surface.

Our estimation of the instantaneous TOA DRE<sub>sw</sub> efficiency is in reasonable agreement with the values reported in a recent study by Mishra et al. [2017]. Their observations are from a satellite instrument similar to CERES, called Megha-Tropiques-ScaRaB (MT- ScaRaB). Flying in a low-inclination orbit, this instrument is able to observe the TOA radiation in the tropical region at various local times. Using 4 years MT- ScaRaB radiation and MODIS AOD observation, Mishra et al. [2017] estimate that the instantaneous TOA DRE<sub>sw</sub> corresponding to a solar zenith angle of  $\sim 40^\circ$  in the North Atlantic region is about  $-40 \pm 3$  W/m<sup>2</sup>/AOD, which is in between our range of  $-49.7 \pm 7.1$  W/m<sup>2</sup>/AOD and  $-36.5 \pm 4.8$  W/m<sup>2</sup>/AOD. Our estimation of the diurnal mean TOA DRE<sub>sw</sub> efficiency ( $-28$  W/m<sup>2</sup>/AOD) is in between the  $-18$  W/m<sup>2</sup>/AOD reported in Mishra et al. [2017] and  $-35$  W/m<sup>2</sup>/AOD reported in Li et al. [2004]. The difference may result from different



601 selection of cases and domain. Note that our analysis is limited to cloud-free and dust-dominant  
602 cases that are selected based on MODIS and CALIOP observations.

603         Due to the lack of study on dust  $DRE_{LW}$  in this region, it is difficult to find a comparable  
604 result the literature to validate our estimate of  $DRE_{LW}$ . Nevertheless, our result that the positive  
605  $DRE_{LW}$  cancels about 30% of the negative  $DRE_{SW}$  in the computation of the diurnal mean net dust  
606 DRE is in agreement with many previous studies attesting the importance of dust  $DRE_{LW}$  (e.g.,  
607 Zhang et al. 2003, Haywood et al. 2005). Note that over land, e.g., the Sahara Desert, the brighter  
608 surface reflectance will reduce the cooling effect of  $DRE_{SW}$  or even leads to warming (positive)  
609  $DRE_{SW}$ . At the same time, the hot surface temperature during daytime may result in  $DRE_{LW}$   
610 significantly larger than that over ocean. Therefore, the  $DRE_{LW}$  is expected to be even more  
611 significant in comparison with  $DRE_{SW}$ , over land than over ocean, which is an interesting topic for  
612 future studies.

613         Another interesting result from this study is that given the same visible AOD dust particle  
614 size and dust absorption in the SW can compromise each other in determining dust  $DRE_{SW}$ . As a  
615 result, it is difficult to specify both variables using the SW radiation alone. In such case, the LW  
616 radiation could provide complementary and important information on dust properties, especially  
617 dust particle size. Most of the current aerosol property retrieval algorithms use only SW radiation  
618 observations. There are also a few algorithms to retrieve dust properties using only LW radiation  
619 observation [e.g., Pierangelo et al., 2004, DeSouza-Machado et al. 2006, Peyridieu et al., 2010].  
620 It is worth exploring in future studies the possibility and benefit of retrieving dust properties  
621 utilizing both the SW and LW observations.

622



623

## 624 Figures and Tables:

625

626

627 Table 1 Observation-based instantaneous (at A-Train overpassing time) DRE and DRE<sub>sw</sub>  
 628 Efficiency at the top of atmosphere (TOA). The values in the parenthesis for DRE<sub>LW</sub> are based  
 629 on the assumption of 0.7 W/m<sup>2</sup> bias in our clear-sky OLR computation. See text for detail.

630

	TOA DRE <sub>sw</sub> Efficiency [W · m <sup>-2</sup> · AOD <sup>-1</sup> ]	TOA DRE <sub>sw</sub> [W · m <sup>-2</sup> ]	TOA DRE <sub>LW</sub> [W · m <sup>-2</sup> ]
CERES-MODIS AOD	-49.7±7.1	-14.2±2.0	3.1±0.60 (2.4±0.60)
CERES-CALIPSO AOD	-36.5±4.8	-10.4±1.4	3.4±0.32 (2.7±0.32)

631

632

633

634

635

636

637

638

639

640

641

642

643

644

645

646

647

648

649

650

651

652

653

654

655

656

657



658

659

660

661 Table 2 Instantaneous  $DRE_{sw}$  and  $DRE_{sw}$  Efficiency at TOA and Surface based on different  
662 dust models (e.g., PSD, refractive index, and shape).

PSD	Refractive index	Shape	TOA $DRE_{sw}$ Efficiency ( $W/m^2/AOD$ )	TOA $DRE_{sw}$ ( $W/m^2$ )	Surface $DRE_{sw}$ Efficiency ( $W/m^2/AOD$ )	Surface $DRE_{sw}$ ( $W/m^2$ )
Fennec-SAL	Colarco-SW	Dubovik	-47.6	-13.5	-179.4	-51.5
AERONET	OPAC-SW	Dubovik	-53.3	-15.5	-190.1	-55.0
Fennec-SAL	Colarco-SW	Spherical	-39.8	-11.4	-200.4	-58.2

663

664

665



666  
 667 Table 3 Instantaneous  $DRE_{LW}$  based on different dust models. Note that the diurnal mean values  
 668 are almost identical to the instantaneous results due to small diurnal variation in the LW.

PSD	Refractive index	Shape	TOA $DRE_{LW}$ (W/m <sup>2</sup> )	Surface $DRE_{LW}$ (W/m <sup>2</sup> )
Fennec-SAL	OPAC-LW	Dubovik	3.0	7.7
AERONET	OPAC-LW	Dubovik	1.8	4.7
Fennec-SAL	Di-Biagio-LW	Dubovik	2.4	5.4
Fennec-SAL	OPAC-LW	Spherical	3.6	9.4

669  
 670  
 671



672  
673 Table 4 The difference in OLR between our computations and the CERES measurements for the  
674 selected dust cases. The values in the parenthesis are based on the assumption of  $0.7 \text{ W/m}^2$  bias  
675 in our clear-sky OLR computation.

PSD	Refractive index	shape	Mean Difference	Standard Deviation	t-score	p-value
Fennec -SAL	OPAC-LW	Dubovik	0.5 (-0.2)	3.8	1.2 (-0.62)	0.23 (0.55)
Fennec-SAL	Di-Biagio-LW	Dubovik	1.0 (0.3)	3.7	2.67 (0.83)	0.008 (0.41)
AERONET	OPAC-LW	Dubovik	1.6 (0.9)	3.7	4.21 (2.36)	$2.7\text{e-}5$ (0.02)
AERONET	Di-Biagio-LW	Dubovik	2.2 (1.5)	3.7	5.82 (3.94)	$7.7\text{e-}9$ ( $8.5\text{e-}5$ )

676  
677





678  
 679 Table 5 OLR computations based on different dust shape models. The values in the parenthesis  
 680 for  $DRE_{LW}$  are based on the assumption of  $0.7 \text{ W/m}^2$  bias in our clear-sky OLR computation.  
 681

PSD	Refractive index	shape	Mean Difference	Standard Deviation	t-score	p-value
Fennec-SAL	OPAC-LW	Dubovik	0.5 (-0.2)	3.8	1.2 (-0.62)	0.23 (0.54)
Fennec-SAL	OPAC-LW	Kandler	0.3 (-0.4)	3.9	0.9 (-0.90)	0.36 (0.37)
Fennec-SAL	OPAC-LW	Sphere	-0.1 (-0.8)	4.0	-0.35 (-2.1)	0.73 (0.033)

682  
 683



684

685 Table 6 Diurnally mean  $DRE_{sw}$  and  $DRE_{sw}$  Efficiency at TOA and Surface

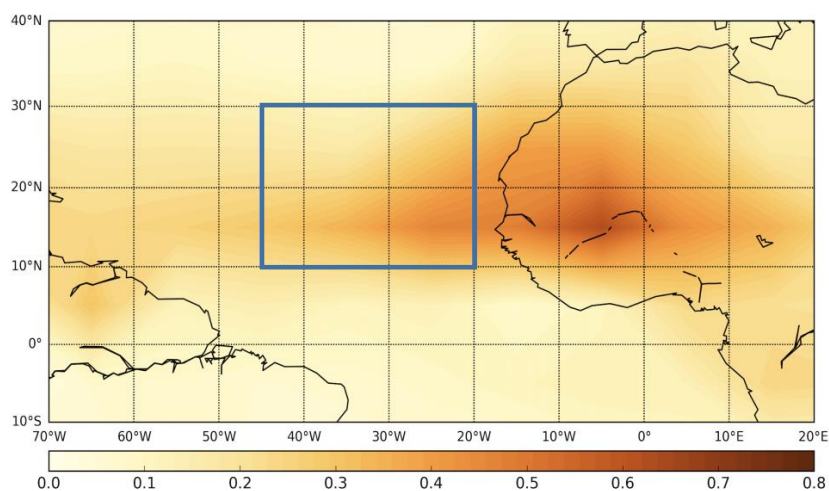
PSD	Refractive index	Shape	TOA $DRE_{sw}$ Efficiency ( $W/m^2/AOD$ )	TOA $DRE_{sw}$ ( $W/m^2$ )	Surface $DRE_{sw}$ Efficiency ( $W/m^2/AOD$ )	Surface $DRE_{sw}$ ( $W/m^2$ )
Fennec-SAL	Colarco-SW	Dubovik	-28	-9.9	-82.1	-26.0
AERONET	OPAC-SW	Dubovik	-29.4	-10.3	-85.7	-27.2
Fennec-SAL	Colarco-SW	Spherical	-22.8	-8.2	-89.6	-28.5

686

687



688  
 689  
 690  
 691  
 692  
 693  
 694  
 695  
 696  
 697  
 698  
 699  
 700  
 701  
 702  
 703  
 704  
 705  
 706  
 707  
 708  
 709  
 710  
 711



712  
 713 Figure 1 CALIPSO derived seasonal mean (JJA) dust aerosol optical depth (AOD) at 0.5  $\mu\text{m}$   
 714 averaged over five summers (2007~2011) in cloud free sky condition from the integrated  
 715 CALIPSO, CloudSat, CERES, MODIS merged product (CCCM).

716  
 717

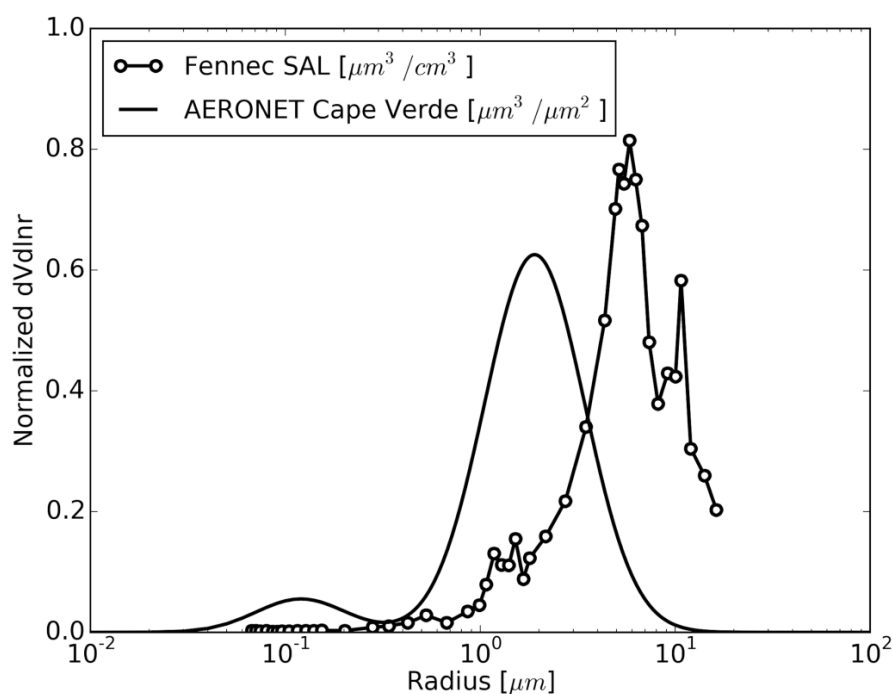


Figure 2 Size distributions of mineral dust used in this study. Fennec-SAL curve is from a new in-situ measurement of Saharan dust taken during the Fennec 2011 aircraft campaign [Ryder et al. 2013]. The solid curve represents desert dust size distribution retrieved from AERONET observations at Cape Verde site reported in Dubovik et al. [2002].

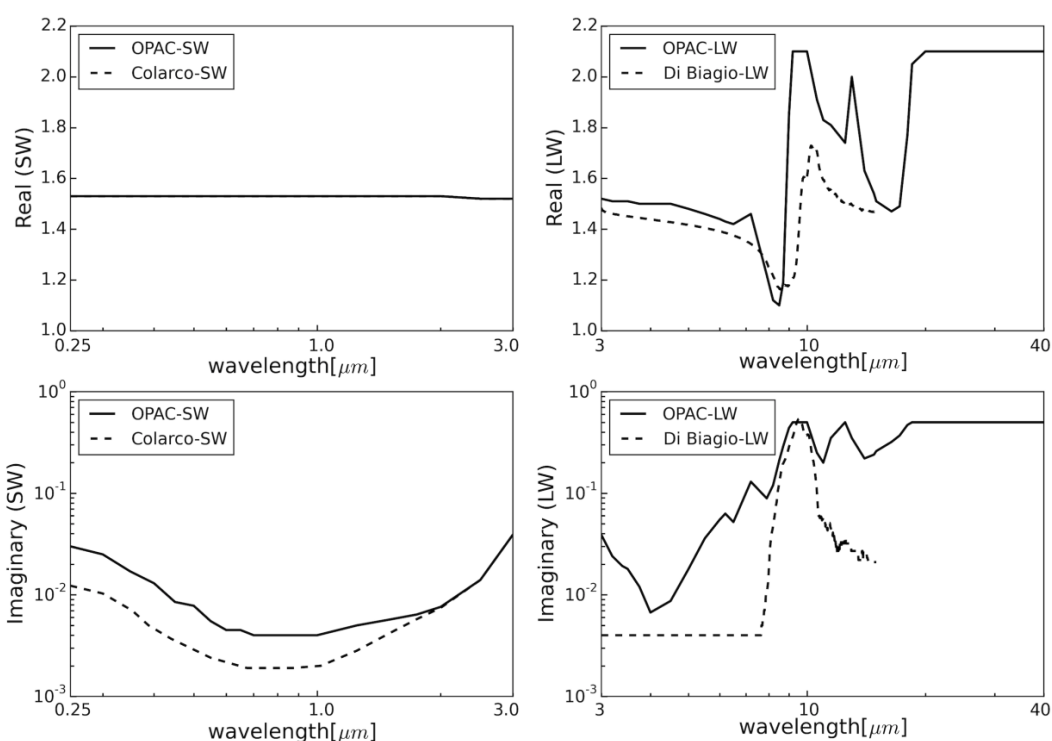


Figure 3 a) real and b) imaginary part of the SW dust refractive index from OPAC [Hess et al. 1998] and Colarco et al. [2014]; c) real and d) imaginary part of the LW dust refractive index from OPAC [Hess et al. 1998] and Di Biagio o et al. [2016].

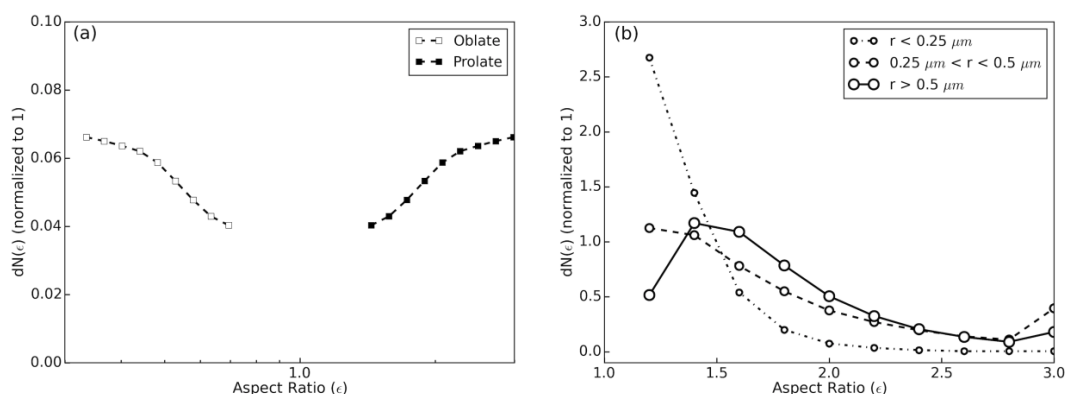


Figure 4 Two spheroidal dust shape distributions models a) shows aspect ratio distributions from Dubovik et al. [2006]. The  $\ln \epsilon$ -interval is 0.09. b) shows aspect ratio distributions as function of particle radius interval discretized from measurement of Kandler et al. (2009). The first point of each line covers the measurement data from  $\epsilon = 1.0$  to 1.3, the last point of each line covers  $\epsilon > 2.9$  and the other points cover  $\epsilon$ -intervals of 0.2 Koepke et al. [2015].

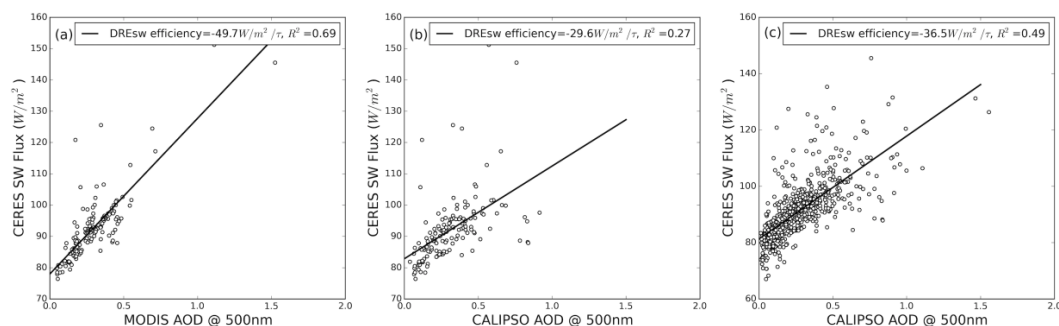


Figure 5 Linear regressions of CERES measured upward SW flux at TOA with satellite retrieved AOD for the selected cloud-free and dust dominant cases. a) shows the combination of CERES and MODIS AOD for 153 cases with both CALIPSO AOD and MODIS AOD retrievals. b) shows the combination of CERES and CALIPSO AOD for 153 cases. c) is for other 454 cases with only CALIPSO AOD retrievals.

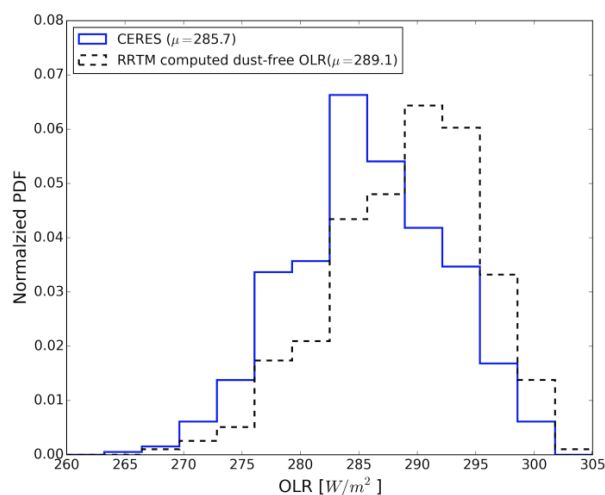


Figure 6 PDF of observed OLR from CERES (i.e., with dust) and computed dust-free OLR based on the atmospheric profiles and surface temperature reported in CCCM.



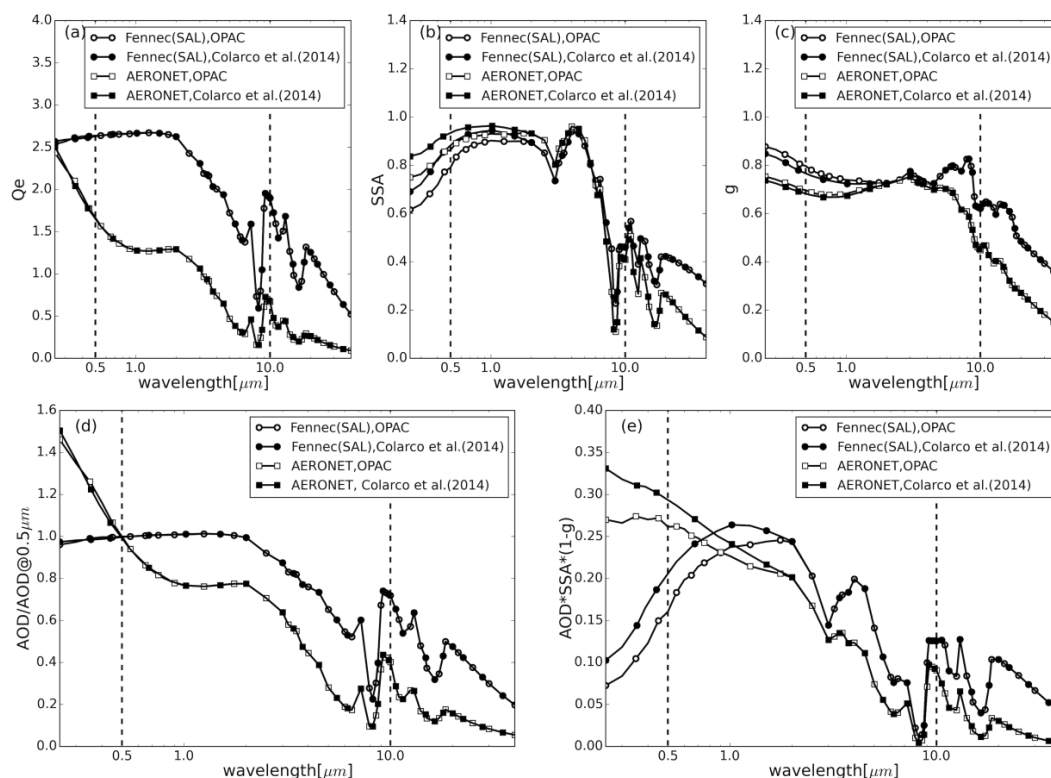


Figure 7 a) Extinction efficiency ( $Q_e$ ), b) single scattering albedo (SSA), c) asymmetry factor ( $g$ ) d) normalized AOD with respect to AOD @  $0.5 \mu\text{m}$ , and e)  $\text{AOD} \cdot \text{SSA} \cdot (1-g)$  of dust aerosols based on different combination of PSD and refractive index. PSD type and refractive index type are indicated in legends.

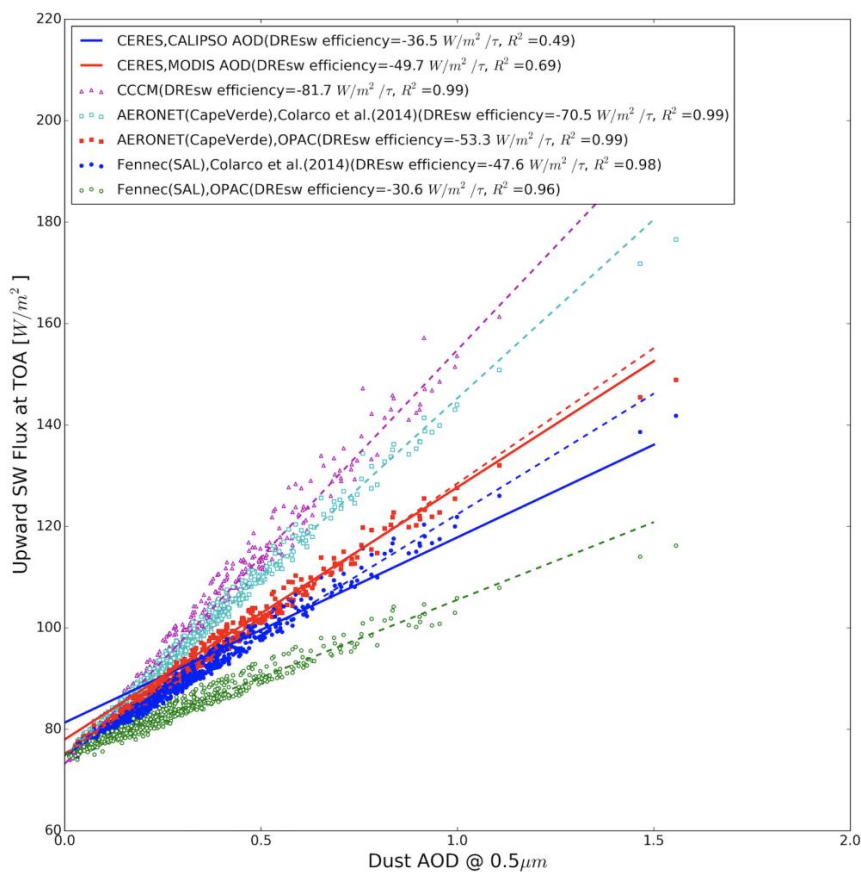


Figure 8 The four sets of simulated TOA upward SW fluxes as a function of the input AOD at 0.5  $\mu\text{m}$ .

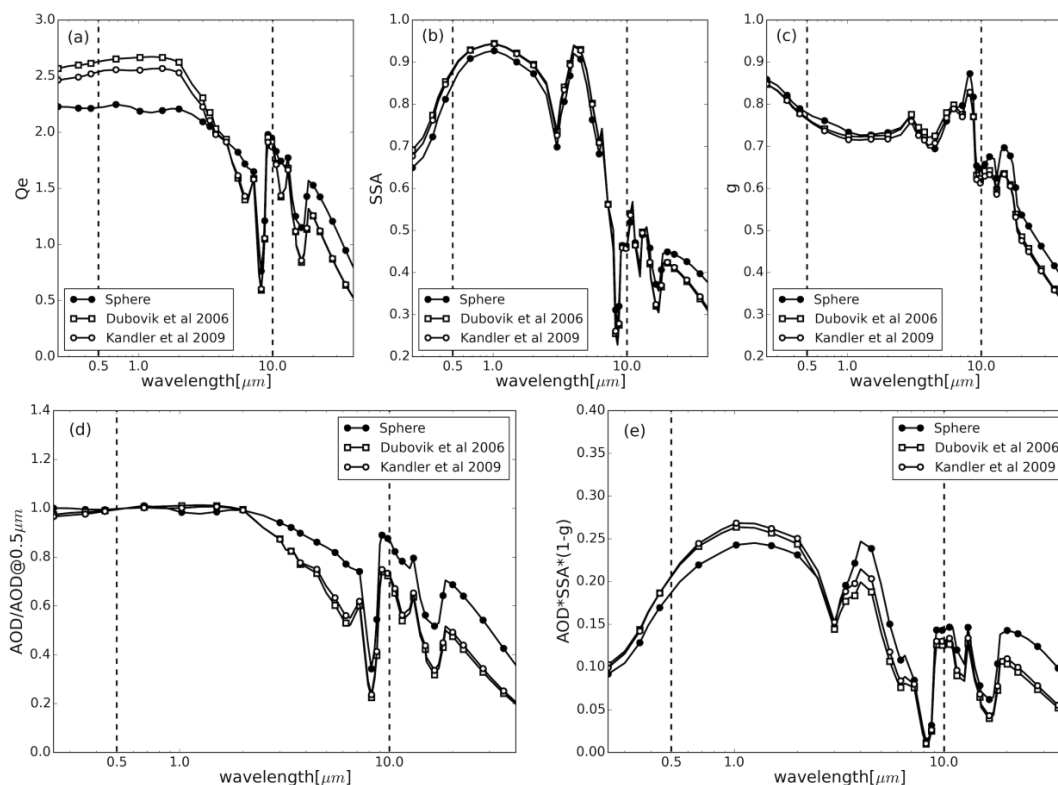
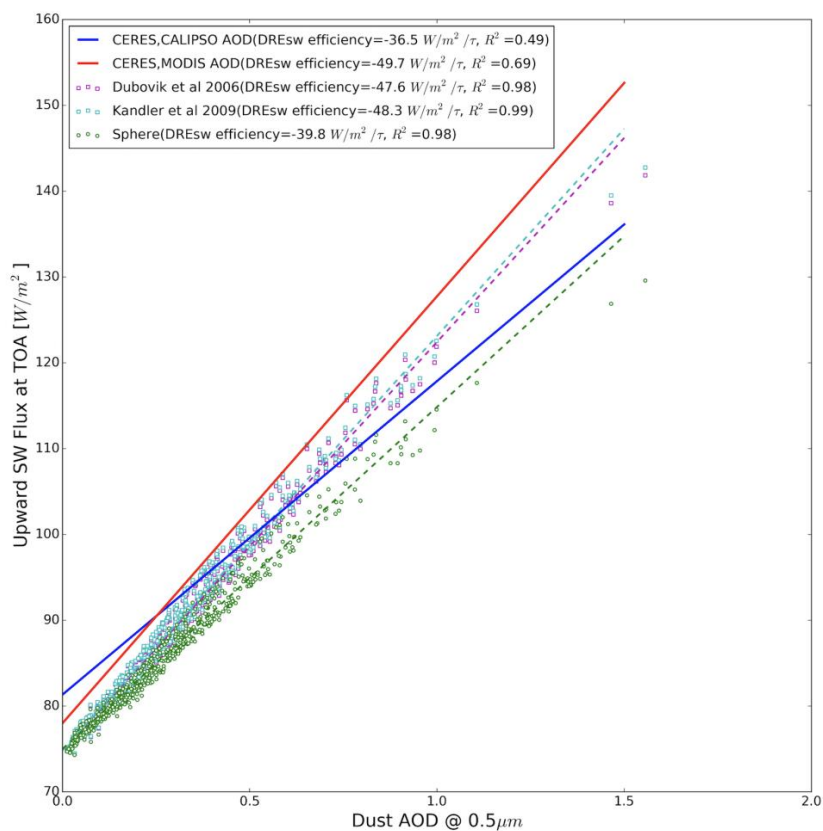


Figure 9 Extinction efficiency (Qe), b) single scattering albedo (SSA), c) asymmetry factor (g) d) normalized AOD with respect to AOD @ 0.5  $\mu\text{m}$ , and e) AOD\*SSA\*(1-g) of dust aerosols based on different combination of PSD and refractive index. PSD type and refractive index type are indicated in legends.



853



854

855

856 *Figure 10 shows the radiative transfer simulations for the selected cases based on the three dust*  
 857 *shape models.*

858

859

860

861

862

863

864

865

866

867

868

869

870

871



872

873 **References:**

- 874 Ackerman, A. S., Toon, O. B., Stevens, D. E., et al., "Reduction of tropical cloudiness by soot",  
875 Science, **288**, 5468, 1042-1047, (2000), doi:DOI 10.1126/science.288.5468.1042.
- 876 Albrecht, B. A., "Aerosols, Cloud Microphysics, and Fractional Cloudiness", Science, **245**, 4923,  
877 1227-1230, (1989), doi:DOI 10.1126/science.245.4923.1227.
- 878 Balkanski, Y., Schulz, M., Claquin, T. and Guibert, S., "Reevaluation of Mineral aerosol  
879 radiative forcings suggests a better agreement with satellite and AERONET data",  
880 Atmospheric Chemistry and Physics, **7**, 81-95, (2007), doi:DOI 10.5194/acp-7-81-2007.
- 881 Carlson, T. N. and Benjamin, S. G., "Radiative Heating Rates for Saharan Dust", Journal of the  
882 Atmospheric Sciences, **37**, 1, 193-213, (1980), doi:Doi 10.1175/1520-  
883 0469(1980)037<0193:Rhfsd>2.0.Co;2.
- 884 Cess, R. D., "Nuclear-War - Illustrative Effects of Atmospheric Smoke and Dust Upon Solar-  
885 Radiation", Climatic Change, **7**, 2, 237-251, (1985), doi:Doi 10.1007/Bf00140508.
- 886 Choobari, O. A., P. Zawar-Reza and Sturman, A., "The global distribution of mineral dust and its  
887 impacts on the climate system: A review", Atmospheric Research, **138**, 152-165, (2014),  
888 doi:10.1016/j.atmosres.2013.11.007.
- 889 Colarco, P. R., Nowottnick, E. P., Randles, C. A., et al., "Impact of radiatively interactive dust  
890 aerosols in the NASA GEOS-5 climate model: Sensitivity to dust particle shape and  
891 refractive index", Journal of Geophysical Research-Atmospheres, **119**, 2, 753-786,  
892 (2014), doi:10.1002/2013jd020046.
- 893 Colarco, P. R., Toon, O. B., Torres, O. and Rasch, P. J., "Determining the UV imaginary index  
894 of refraction of Saharan dust particles from Total Ozone Mapping Spectrometer data  
895 using a three-dimensional model of dust transport", Journal of Geophysical Research-  
896 Atmospheres, **107**, D16, (2002), doi:Artn 4289 10.1029/2001jd000903.
- 897 Collins, W. D., Rasch, P. J., Eaton, B. E., et al., "Simulating aerosols using a chemical transport  
898 model with assimilation of satellite aerosol retrievals: Methodology for INDOEX",  
899 Journal of Geophysical Research-Atmospheres, **106**, D7, 7313-7336, (2001), doi:Doi  
900 10.1029/2000jd900507.
- 901 Cuesta, J., Marsham, J. H., Parker, D. J. and Flamant, C., "Dynamical mechanisms controlling  
902 the vertical redistribution of dust and the thermodynamic structure of the West Saharan  
903 atmospheric boundary layer during summer", Atmospheric Science Letters, **10**, 1, 34-42,  
904 (2009), doi:10.1002/asl.207.
- 905 DeSouza-Machado, S. G., Strow, L. L., Hannon, S. E. and Motteler, H. E., "Infrared dust  
906 spectral signatures from AIRS", Geophysical Research Letters, **33**, 3, (2006), doi:Artn  
907 L03801  
908 10.1029/2005gl024364.
- 909 Di Biagio, C., Formenti, P., Balkanski, Y., et al., "Global scale variability of the mineral dust  
910 long-wave refractive index: a new dataset of in situ measurements for climate modeling  
911 and remote sensing", Atmospheric Chemistry and Physics, **17**, 3, 1901-1929, (2017),  
912 doi:10.5194/acp-17-1901-2017.
- 913 Di Biagio, C., Formenti, P., Styler, S. A., Pangui, E. and Doussin, J. F., "Laboratory chamber  
914 measurements of the longwave extinction spectra and complex refractive indices of  
915 African and Asian mineral dusts", Geophysical Research Letters, **41**, 17, 6289-6297,  
916 (2014), doi:10.1002/2014gl060213.



- 917 Dubovik, O., Holben, B., Eck, T. F., et al., "Variability of absorption and optical properties of  
918 key aerosol types observed in worldwide locations", *Journal of the Atmospheric*  
919 *Sciences*, **59**, 3, 590-608, (2002), doi:Doi 10.1175/1520-  
920 0469(2002)059<0590:Voaaop>2.0.Co;2.
- 921 Dubovik, O., Sinyuk, A., Lapyonok, T., et al., "Application of spheroid models to account for  
922 aerosol particle nonsphericity in remote sensing of desert dust", *Journal of Geophysical*  
923 *Research-Atmospheres*, **111**, D11, (2006), doi:Artn D11208 10.1029/2005jd006619.
- 924 Formenti, P., Schutz, L., Balkanski, Y., et al., "Recent progress in understanding physical and  
925 chemical properties of African and Asian mineral dust", *Atmospheric Chemistry and*  
926 *Physics*, **11**, 16, 8231-8256, (2011), doi:10.5194/acp-11-8231-2011.
- 927 Fouquart, Y., Bonnel, B., Brogniez, G., et al., "Observations of Saharan Aerosols - Results of  
928 Eclats Field Experiment .2. Broad-Band Radiative Characteristics of the Aerosols and  
929 Vertical Radiative Flux Divergence", *Journal of Climate and Applied Meteorology*, **26**, 1,  
930 38-52, (1987), doi:10.1175/1520-0450(1987)026<0038:Oosaro>2.0.Co;2.
- 931 Hansen, J., Sato, M. and Ruedy, R., "Radiative forcing and climate response", *Journal of*  
932 *Geophysical Research-Atmospheres*, **102**, D6, 6831-6864, (1997), doi:Doi  
933 10.1029/96jd03436.
- 934 Hashimoto, M., Nakajima, T., Dubovik, O., et al., "Development of a new data-processing  
935 method for SKYNET sky radiometer observations", *Atmospheric Measurement*  
936 *Techniques*, **5**, 11, 2723-2737, (2012), doi:10.5194/amt-5-2723-2012.
- 937 Hess, M., Koepke, P. and Schult, I., "Optical properties of aerosols and clouds: The software  
938 package OPAC", *Bulletin of the American Meteorological Society*, **79**, 5, 831-844,  
939 (1998), doi:Doi 10.1175/1520-0477(1998)079<0831:Opoaac>2.0.Co;2.
- 940 Hsu, N. C., Herman, J. R. and Weaver, C., "Determination of radiative forcing of Saharan dust  
941 using combined TOMS and ERBE data", *Journal of Geophysical Research-Atmospheres*,  
942 **105**, D16, 20649-20661, (2000), doi:Doi 10.1029/2000jd900150.
- 943 Jickells, T. D., An, Z. S., Andersen, K. K., et al., "Global iron connections between desert dust,  
944 ocean biogeochemistry, and climate", *Science*, **308**, 5718, 67-71, (2005), doi:DOI  
945 10.1126/science.1105959.
- 946 Kandler, K., Schutz, L., Deutscher, C., et al., "Size distribution, mass concentration, chemical  
947 and mineralogical composition and derived optical parameters of the boundary layer  
948 aerosol at Tinfou, Morocco, during SAMUM 2006", *Tellus Series B-Chemical and*  
949 *Physical Meteorology*, **61**, 1, 32-50, (2009), doi:10.1111/j.1600-0889.2008.00385.x.
- 950 Karyampudi, V. M., Palm, S. P., Reagen, J. A., et al., "Validation of the Saharan dust plume  
951 conceptual model using lidar, Meteosat, and ECMWF data", *Bulletin of the American*  
952 *Meteorological Society*, **80**, 6, 1045-1075, (1999), doi:Doi 10.1175/1520-  
953 0477(1999)080<1045:Votsdp>2.0.Co;2.
- 954 Kato, S., Rose, F. G., Sun-Mack, S., et al., "Improvements of top-of-atmosphere and surface  
955 irradiance computations with CALIPSO-, CloudSat-, and MODIS-derived cloud and  
956 aerosol properties", *Journal of Geophysical Research-Atmospheres*, **116**, (2011), doi:Artn  
957 D19209 10.1029/2011jd016050.
- 958 Kato, S., Sun-Mack, S., Miller, W. F., et al., "Relationships among cloud occurrence frequency,  
959 overlap, and effective thickness derived from CALIPSO and CloudSat merged cloud  
960 vertical profiles", *Journal of Geophysical Research-Atmospheres*, **115**, (2010), doi:Artn  
961 D00h28  
962 10.1029/2009jd012277.





- 963 Keil, A. and Haywood, J. M., "Solar radiative forcing by biomass burning aerosol particles  
964 during SAFARI 2000: A case study based on measured aerosol and cloud properties",  
965 Journal of Geophysical Research-Atmospheres, **108**, D13, (2003), doi:Artn 8467  
966 10.1029/2002jhd002315.
- 967 Kim, D., Chin, M., Yu, H., et al., "Dust optical properties over North Africa and Arabian  
968 Peninsula derived from the AERONET dataset", Atmospheric Chemistry and Physics, **11**,  
969 20, 10733-10741, (2011), doi:10.5194/acp-11-10733-2011.
- 970 Koepke, P., Gasteiger, J. and Hess, M., "Technical Note: Optical properties of desert aerosol  
971 with non-spherical mineral particles: data incorporated to OPAC", Atmospheric  
972 Chemistry and Physics, **15**, 10, 5947-5956, (2015), doi:10.5194/acp-15-5947-2015.
- 973 Kok, J. F., Ridley, D. A., Zhou, Q., et al., "Smaller desert dust cooling effect estimated from  
974 analysis of dust size and abundance", Nature Geoscience, **10**, 4, 274+, (2017),  
975 doi:10.1038/Ngeo2912.
- 976 Koren, I., Kaufman, Y. J., Remer, L. A. and Martins, J. V., "Measurement of the effect of  
977 Amazon smoke on inhibition of cloud formation", Science, **303**, 5662, 1342-1345,  
978 (2004), doi:DOI 10.1126/science.1089424.
- 979 Levoni, C., Cervino, M., Guzzi, R. and Torricella, F., "Atmospheric aerosol optical properties: a  
980 database of radiative characteristics for different components and classes", Applied  
981 Optics, **36**, 30, 8031-8041, (1997), doi:Doi 10.1364/Ao.36.008031.
- 982 Levy, R. C., Remer, L. A., Mattoo, S., Vermote, E. F. and Kaufman, Y. J., "Second-generation  
983 operational algorithm: Retrieval of aerosol properties over land from inversion of  
984 Moderate Resolution Imaging Spectroradiometer spectral reflectance", Journal of  
985 Geophysical Research-Atmospheres, **112**, D13, (2007), doi:Artn D13211  
986 10.1029/2006jd007811.
- 987 Li, F., Vogelmann, A. M. and Ramanathan, V., "Saharan dust aerosol radiative forcing measured  
988 from space", Journal of Climate, **17**, 13, 2558-2571, (2004), doi:Doi 10.1175/1520-  
989 0442(2004)017<2558:Sdarfm>2.0.Co;2.
- 990 Liao, H. and Seinfeld, J. H., "Radiative forcing by mineral dust aerosols: sensitivity to key  
991 variables", Journal of Geophysical Research-Atmospheres, **103**, D24, 31637-31645,  
992 (1998), doi:10.1029/1998jd200036.
- 993 Liu, Z. Y., Omar, A., Vaughan, M., et al., "CALIPSO lidar observations of the optical properties  
994 of Saharan dust: A case study of long-range transport", Journal of Geophysical Research-  
995 Atmospheres, **113**, D7, (2008), doi:Artn D07207 10.1029/2007jd008878.
- 996 Mahowald, N., Albani, S., Kok, J. F., et al., "The size distribution of desert dust aerosols and its  
997 impact on the Earth system", Aeolian Research, **15**, 53-71, (2014),  
998 doi:10.1016/j.aeolia.2013.09.002.
- 999 Maring, H., Savoie, D. L., Izaguirre, M. A., Custals, L. and Reid, J. S., "Mineral dust aerosol size  
1000 distribution change during atmospheric transport", Journal of Geophysical Research-  
1001 Atmospheres, **108**, D19, (2003), doi:Artn 8592 10.1029/2002jd002536.
- 1002 McCormick, R. A. and Ludwig, J. H., "Climate Modification by Atmospheric Aerosols",  
1003 Science, **156**, 3780, 1358+, (1967), doi:DOI 10.1126/science.156.3780.1358.
- 1004 Meng, Z. K., Yang, P., Kattawar, G. W., et al., "Single-scattering properties of tri-axial  
1005 ellipsoidal mineral dust aerosols: A database for application to radiative transfer  
1006 calculations", Journal of Aerosol Science, **41**, 5, 501-512, (2010),  
1007 doi:10.1016/j.jaerosci.2010.02.008.



- 1008 Mishchenko, M. I., Travis, L. D., Kahn, R. A. and West, R. A., "Modeling phase functions for  
1009 dustlike tropospheric aerosols using a shape mixture of randomly oriented polydisperse  
1010 spheroids", *Journal of Geophysical Research-Atmospheres*, **102**, D14, 16831-16847,  
1011 (1997), doi:Doi 10.1029/96jd02110.
- 1012 Mishra, M. K., Gupta, A. K. and Rajeev, K., "Spaceborne Observations of the Diurnal Variation  
1013 of Shortwave Aerosol Direct Radiative Effect at Top of Atmosphere Over the Dust-  
1014 Dominated Arabian Sea and the Atlantic Ocean", *Ieee Transactions on Geoscience and  
1015 Remote Sensing*, **55**, 11, 6610-6616, (2017), doi:10.1109/Tgrs.2017.2730758.
- 1016 Mlawer, E. J., Taubman, S. J., Brown, P. D., Iacono, M. J. and Clough, S. A., "Radiative transfer  
1017 for inhomogeneous atmospheres: RRTM, a validated correlated-k model for the  
1018 longwave", *Journal of Geophysical Research-Atmospheres*, **102**, D14, 16663-16682,  
1019 (1997), doi:Doi 10.1029/97jd00237.
- 1020 Myhre, G., Grini, A., Haywood, J. M., et al., "Modeling the radiative impact of mineral dust  
1021 during the Saharan Dust Experiment (SHADE) campaign", *Journal of Geophysical  
1022 Research-Atmospheres*, **108**, D18, (2003), doi:Artn 8579 10.1029/2002jd002566.
- 1023 Peyridieu, S., Chedin, A., Tanre, D., et al., "Saharan dust infrared optical depth and altitude  
1024 retrieved from AIRS: a focus over North Atlantic - comparison to MODIS and  
1025 CALIPSO", *Atmospheric Chemistry and Physics*, **10**, 4, 1953-1967, (2010),  
1026 doi:10.5194/acp-10-1953-2010.
- 1027 Pierangelo, C., Chedin, A., Heilliette, S., Jacquinet-Husson, N. and Armante, R., "Dust altitude  
1028 and infrared optical depth from AIRS", *Atmospheric Chemistry and Physics*, **4**, 1813-  
1029 1822, (2004), doi:10.5194/acp-4-1813-2004.
- 1030 Platnick, S., King, M. D., Ackerman, S. A., et al., "The MODIS cloud products: Algorithms and  
1031 examples from Terra", *Ieee Transactions on Geoscience and Remote Sensing*, **41**, 2, 459-  
1032 473, (2003), doi:10.1109/Tgrs.2002.808301.
- 1033 Rajot, J. L., Formenti, P., Alfaro, S., et al., "AMMA dust experiment: An overview of  
1034 measurements performed during the dry season special observation period (SOP0) at the  
1035 Banizoumbou (Niger) supersite", *Journal of Geophysical Research-Atmospheres*, **113**,  
1036 D20, (2008), doi:Artn D00c14 10.1029/2008jd009906.
- 1037 Ramaswamy, V. and Kiehl, J. T., "Sensitivities of the Radiative Forcing Due to Large Loadings  
1038 of Smoke and Dust Aerosols", *Journal of Geophysical Research-Atmospheres*, **90**, Nd3,  
1039 5597-5613, (1985), doi:DOI 10.1029/JD090iD03p05597.
- 1040 Remer, L. A., Kaufman, Y. J., Tanre, D., et al., "The MODIS aerosol algorithm, products, and  
1041 validation", *Journal of the Atmospheric Sciences*, **62**, 4, 947-973, (2005), doi:Doi  
1042 10.1175/Jas3385.1.
- 1043 Rienecker, M. M., Suarez, M. J., Todling, R., et al., "The GEOS-5 data assimilation system -  
1044 Documentation of versions 5.0.1, 5.1.0, and 5.2.0", *NASA Tech. Memo.*, **27**, (2008).
- 1045 Rosenfeld, D. and Lensky, I. M., "Satellite-based insights into precipitation formation processes  
1046 in continental and maritime convective clouds", *Bulletin of the American Meteorological  
1047 Society*, **79**, 11, 2457-2476, (1998), doi:Doi 10.1175/1520-  
1048 0477(1998)079<2457:Sbiipf>2.0.Co;2.
- 1049 Ryder, C. L., Highwood, E. J., Lai, T. M., Sodemann, H. and Marsham, J. H., "Impact of  
1050 atmospheric transport on the evolution of microphysical and optical properties of Saharan  
1051 dust", *Geophysical Research Letters*, **40**, 10, 2433-2438, (2013a), doi:10.1002/grl.50482.
- 1052 Ryder, C. L., Highwood, E. J., Rosenberg, P. D., et al., "Optical properties of Saharan dust  
1053 aerosol and contribution from the coarse mode as measured during the Fennec 2011





- 1054 aircraft campaign", *Atmospheric Chemistry and Physics*, **13**, 1, 303-325, (2013b),  
1055 doi:10.5194/acp-13-303-2013.
- 1056 Ryder, C. L., McQuaid, J. B., Flamant, C., et al., "Advances in understanding mineral dust and  
1057 boundary layer processes over the Sahara from Fennec aircraft observations",  
1058 *Atmospheric Chemistry and Physics*, **15**, 14, 8479-8520, (2015), doi:10.5194/acp-15-  
1059 8479-2015.
- 1060 Sokolik, I. N. and Toon, O. B., "Direct radiative forcing by anthropogenic airborne mineral  
1061 aerosols", *Nature*, **381**, 6584, 681-683, (1996), doi:DOI 10.1038/381681a0.
- 1062 Sokolik, I. N. and Toon, O. B., "Incorporation of mineralogical composition into models of the  
1063 radiative properties of mineral aerosol from UV to IR wavelengths", *Journal of*  
1064 *Geophysical Research-Atmospheres*, **104**, D8, 9423-9444, (1999), doi:Doi  
1065 10.1029/1998jd200048.
- 1066 Sokolik, I. N., Toon, O. B. and Bergstrom, R. W., "Modeling the radiative characteristics of  
1067 airborne mineral aerosols at infrared wavelengths", *Journal of Geophysical Research-*  
1068 *Atmospheres*, **103**, D8, 8813-8826, (1998), doi:Doi 10.1029/98jd00049.
- 1069 Stegmann, P. G. and Yang, P., "A regional, size-dependent, and causal effective medium model  
1070 for Asian and Saharan mineral dust refractive index spectra", *Journal of Aerosol Science*,  
1071 **114**, 327-341, (2017), doi:10.1016/j.jaerosci.2017.10.003.
- 1072 Tegen, I. and Lacis, A. A., "Modeling of particle size distribution and its influence on the  
1073 radiative properties of mineral dust aerosol", *Journal of Geophysical Research-*  
1074 *Atmospheres*, **101**, D14, 19237-19244, (1996), doi:Doi 10.1029/95jd03610.
- 1075 Tegen, I., Lacis, A. A. and Fung, I., "The influence on climate forcing of mineral aerosols from  
1076 disturbed soils", *Nature*, **380**, 6573, 419-422, (1996), doi:10.1038/380419a0.
- 1077 Textor, C., Schulz, M., Guibert, S., et al., "Analysis and quantification of the diversities of  
1078 aerosol life cycles within AeroCom", *Atmospheric Chemistry and Physics*, **6**, 1777-1813,  
1079 (2006).
- 1080 Twomey, S., "The influence of pollution on the shortwave albedo of clouds", *Journal of the*  
1081 *atmospheric sciences*, **34**, 7, 1149-1152, (1977).
- 1082 Volz, F. E., "Infrared Optical-Constants of Ammonium Sulfate, Sahara Dust, Volcanic Pumice,  
1083 and Flyash", *Applied Optics*, **12**, 3, 564-568, (1973), doi:10.1364/Ao.12.000564.
- 1084 Volz, F. E., "Infrared Refractive-Index of Atmospheric Aerosol Substances", *Applied Optics*, **11**,  
1085 4, 755-759, (1972), doi:Doi 10.1364/Ao.11.000755.
- 1086 Washington, R., Todd, M., Middleton, N. J. and Goudie, A. S., "Dust-storm source areas  
1087 determined by the total ozone monitoring spectrometer and surface observations", *Annals*  
1088 *of the Association of American Geographers*, **93**, 2, 297-313, (2003), doi:Doi  
1089 10.1111/1467-8306.9302003.
- 1090 Weinzierl, B., Ansmann, A., Prospero, J. M., et al., "THE SAHARAN AEROSOL LONG-  
1091 RANGE TRANSPORT AND AEROSOL-CLOUD-INTERACTION EXPERIMENT  
1092 Overview and Selected Highlights", *Bulletin of the American Meteorological Society*, **98**,  
1093 7, 1427-1451, (2017), doi:10.1175/Bams-D-15-00142.1.
- 1094 Weinzierl, B., Sauer, D., Esselborn, M., et al., "Microphysical and optical properties of dust and  
1095 tropical biomass burning aerosol layers in the Cape Verde region-an overview of the  
1096 airborne in situ and lidar measurements during SAMUM-2", *Tellus Series B-Chemical*  
1097 *and Physical Meteorology*, **63**, 4, 589-618, (2011), doi:10.1111/j.1600-  
1098 0889.2011.00566.x.



- 1099 Winker, D. M., Pelon, J., Coakley, J. A., et al., "THE CALIPSO MISSION A Global 3D View of  
1100 Aerosols and Clouds", *Bulletin of the American Meteorological Society*, **91**, 9, 1211-  
1101 1229, (2010), doi:10.1175/2010bams3009.1.
- 1102 Wiscombe, W. J., "Improved Mie Scattering Algorithms", *Applied Optics*, **19**, 9, 1505-1509,  
1103 (1980), doi:10.1364/Ao.19.001505.
- 1104 Yu, H., Kaufman, Y. J., Chin, M., et al., "A review of measurement-based assessments of the  
1105 aerosol direct radiative effect and forcing", *Atmospheric Chemistry and Physics*, **6**, 613-  
1106 666, (2006).
- 1107 Yu, H. B., Chin, M., Yuan, T. L., et al., "The fertilizing role of African dust in the Amazon  
1108 rainforest: A first multiyear assessment based on data from Cloud-Aerosol Lidar and  
1109 Infrared Pathfinder Satellite Observations", *Geophysical Research Letters*, **42**, 6, 1984-  
1110 1991, (2015), doi:10.1002/2015gl063040.
- 1111 Zhang, Z. B., Meyer, K., Yu, H. B., et al., "Shortwave direct radiative effects of above-cloud  
1112 aerosols over global oceans derived from 8 years of CALIOP and MODIS observations",  
1113 *Atmospheric Chemistry and Physics*, **16**, 5, 2877-2900, (2016), doi:10.5194/acp-16-  
1114 2877-2016.
- 1115 Zhou, M., Yu, H., Dickinson, R. E., Dubovik, O. and Holben, B. N., "A normalized description  
1116 of the direct effect of key aerosol types on solar radiation as estimated from Aerosol  
1117 Robotic Network aerosols and Moderate Resolution Imaging Spectroradiometer albedos",  
1118 *Journal of Geophysical Research-Atmospheres*, **110**, D19, (2005), doi:10.1029/2005jd005909.  
1119  
1120  
1121  
1122